Eur. Phys. J. B (2019) 92: 62
https://doi.org/10.1140/epjb/e2018-90346-7

THE EUROPEAN
PHYSICAL JOURNAL B

Colloquium

Cooperative magnetic phenomena in artificial spin systems: spin liquids, Coulomb phase and fragmentation of magnetism – a colloquium

Nicolas Rougemaille[a] and Benjamin Canals

Univ. Grenoble Alpes, CNRS, Institut NEEL, Grenoble INP, 38000 Grenoble, France

Received 29 May 2018 / Received in final form 2 November 2018

Abstract. Two-dimensional arrays of interacting magnetic nanostructures offer a remarkable playground for simulating, experimentally, lattice spin models. Initially designed to capture the low-energy physics of highly frustrated magnets, they quickly became a lab-on-chip platform to investigate cooperative magnetic phenomena often associated with classical frustrated magnetism. This article reviews the many-body physics which can be visualized, directly in real space, through the magnetic imaging of artificial arrays of magnetic nanostructures. Particular attention is paid to classical spin liquid states, magnetic Coulomb phases and magnetic moment fragmentation. Other phenomena, such as complex magnetic ordering, charge crystallization and monopole-like excitations, are also described in light of the recent advances in the field.

1 Introduction

Artificially designed systems often provide a powerful experimental platform to explore, model and challenge the properties of matter. They may also provide an alternative viewpoint compared to other experimental approaches investigating natural systems with their whole complexity. In fact, being able to fabricate a synthetic system to capture a given phenomenon or property is a kind of measure of how deep our knowledge is of this phenomenon or property. Differences between how an artificial system behaves and how its natural counterpart actually behaves, generally leads to very useful pieces of information. Artificial systems may also be fabricated to explore intriguing or exotic effects, which do not exist in nature or which would be too difficult to study otherwise. In that sense, artificial systems may be seen as experimental simulators of matter, complementing what theoretical models and numerical methods can bring.

In magnetism, lithographically-patterned arrays of superconducting architectures [1–7], macroscopic compass needle systems [8–10] and two-dimensional binary alloys [11–15] were introduced in the nineties as a possible way to fabricate various types of spin models. These works were later extended to artificial arrays of interacting nanomagnets [16–18] and colloidal systems [19–23]. This idea to use lithographically patterned architectures, be they magnetic or not, triggered a wealth of studies on spin systems. While they were initially made to mimic the exotic physics of certain compounds [18], their flexibility, tunability and ease of fabrication allowed testing and revisiting many predictions from spin models, but also to explore the many-body physics of systems having no equivalent natural counterparts. Although a wide variety of two-dimensional spin systems can be designed experimentally, most of the work done so far, including what is presented here, addresses the physics of frustrated spin systems, with the aim of investigating the associated exotic physics through a lab-on-chip approach.

The concept of frustration in magnetism was initially introduced for spin glasses [24–26] to account for the impossibility in these systems to satisfy at the same time all exchange interactions due to structural disorder. In the context of frustrated magnets, whether they are artificial or natural compounds, systems have no (or negligible) structural or chemical disorder, and frustration between interacting spins arises from the lattice geometry. The textbook example of a geometrically frustrated spin system is the classical Ising antiferromagnet on a triangular lattice (see Fig. 1a). In that case, the antiferromagnetic bonds between nearest-neighbor spins, together with the odd number of corners in a triangle, lead to the impossibility to minimize simultaneously all pairwise spin interactions. The lowest possible energy for a given triangle is obtained when it hosts one frustrated bond only. Higher energy configurations are obtained when all three bonds are frustrated, i.e., when all spins are ferromagnetically coupled. For one single triangle, the ground state (GS) configuration is thus six times degenerate, while the

---

[a] e-mail: nicolas.rougemaille@neel.cnrs.fr

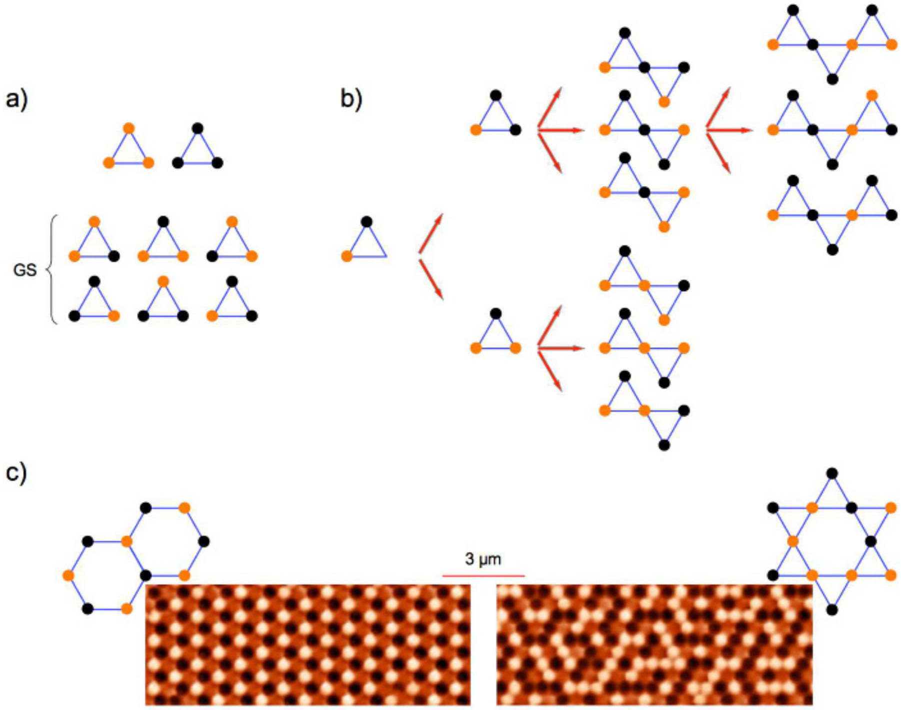

Fig. 1. (a) The eight possible spin states of a triangle, in which the Ising spins are coupled antiferromagnetically. Black and orange circles represent 'up' and 'down' spins, respectively. Six configurations have one frustrated bond. They all have the same lowest possible energy and thus define the ground state (GS). Two other configurations have three frustrated bonds and correspond to a high energy state. (b) Building a chain of corner-sharing triangles leads to a large amount of configurations belonging to the ground state manifold. In fact, the number of low-energy configurations increases exponentially with the length of the chain. (c) Room temperature magnetic force microscopy images of two artificial, two-dimensional Ising spin systems with antiferromagnetic interactions. Black and white contrasts give the local direction of magnetization, either 'up' or 'down', perpendicular to the lattice plane (the nonmagnetic substrate appears in orange). In the left image, the lattice is hexagonal. Because of the even number of corners in a hexagon, the system is not frustrated and shows almost perfect antiferromagnetic ordering (alternation of black and white contrasts between neighboring nanomagnets). In the right image, the lattice has a kagome geometry and the configuration is disordered, because of the odd number of corners in a triangle. Both arrays have felt the exact same field demagnetization protocol to be brought in these arrested configurations.

excited states are twofold degenerate (see Fig. 1a). Building a chain of corner-sharing triangles (Fig. 1b) reveals that the degeneracy of the ground state increases faster than the system size. The ground state of such a chain is said to be macroscopically degenerate as the number of states belonging to the ground state manifold increases exponentially with the length of the chain. In other words, although the system considered here is disorder-free from a structural point of view, it is extensively, magnetically disordered. Because of this extensive degeneracy, the statistical entropy per site remains finite, even at zero temperature, thus contradicting the third law of thermodynamics in its generally formulated expression (Planck formulation, see Ref. [27] for more details). Assuming no energy barrier for flipping a spin in the triangular chain, such a system is never frozen: spins always fluctuate, even at very low temperature, without the need of energy input.

This highly fluctuating magnetic state is not specific to the antiferromagnetic Ising triangular chain, and highly disordered manifolds can be observed in a large variety of one-, two- and three-dimensional spin lattices, for both antiferromagnetic and ferromagnetic interactions between nearest neighboring spins, and for different types of spins (spins do not have to be necessarily Ising-like variables and not even classical objects). However, the lattice geometry is often a key ingredient to induce magnetic frustration, even though the geometry alone cannot be the source of frustration: only the combination of geometry, type of spin and nature of the spin–spin interaction may lead to geometrical frustration. The importance of this combination can be illustrated by considering Ising spins, coupled antiferromagnetically, and placed on a hexagon, a square and a triangle. Because of the even number of bonds in the hexagon and square, no frustration occurs, contrary to the triangle. At the scale of a lattice, the difference between a hexagonal and a kagome lattice is striking (see Fig. 1c): the former shows almost perfect antiferromagnetic ordering after being submitted to a demagnetization protocol (see Sect. 2), while the latter is magnetically disordered after having felt the very same protocol.

One key question that arises when studying geometrically frustrated magnetic systems is how the spins accommodate the frustration, locally, but globally as well. As a matter of fact, probing individual magnetic moments in bulk compounds, without altering the state of the system, is challenging, if even possible. This is precisely where artificial spin systems might be useful. Artificial arrays of magnetic nanostructures can be imaged routinely using standard imaging techniques, such as magnetic force microscopy or X-ray photoemission electron microscopy. These techniques allow the magnetic imaging of global configurations with nanomagnet resolution, i.e., the magnetic state of all individual magnetic elements in the lattice is determined unambiguously, thus permitting the observation of how spins arrange themselves locally, but at large length scales as well. Contrarily to bulk compounds (see for example Ref. [28]) that exhibit exotic properties at very low temperatures (about 1 K), artificial arrays of nanomagnets also present the appealing advantage of being accessible at or near room temperature (in fact this temperature is also tunable at will).

For a theoretician as well as for an experimentalist, it seems difficult to ask for more: all the quantities likely to be evaluated by numerical approaches then become accessible through the magnetic imaging of artificial arrays. This is certainly the reason why the results obtained in 2005–2006 [16–18] on arrays of nanomagnets triggered a wealth of studies at the frontier between nanomagnetism, condensed matter physics and statistical thermodynamics. The physics of artificial spin systems then became a topic on its own.

The present work does not pretend to be exhaustive. It provides a personal, biased view of what makes artificial spin systems such a rich and fascinating playground for studying frustrated magnetism. In the following, we only consider artificial spin systems based on arrays of interacting magnetic nanostructures. We thus exclude several other types of artificial spin systems, such as colloids and superconducting systems, or arrays of compass needles. This work aims at complementing two previous reviews on the topic [29,30]. Besides, detailed information on the magnetic imaging techniques and nanofabrication processes can be found in reference [31], while possible applications of artificial ferroic systems are presented in reference [32]. The main objective of the current manuscript is to introduce and discuss the many-body physics which can be imaged in artificial frustrated spin systems, in light of the advances made in the field these last few years.

This paper is divided into six sections. The question of whether the physics at play in artificial spin systems is representative of a physics at- or out-of-thermodynamic equilibrium is addressed in Section 2. In particular, we show how this question can be answered simply based on the statistical analysis of a single snapshot of an arrested magnetic configuration. The rest of the paper describes the many-body physics of spin liquid states in kagome and square arrays of nanomagnets. There, we illustrate through a few examples how collective phenomena and exotic properties of frustrated, classical spin systems can be captured within a single magnetic image of a two-dimensional array of nanomagnets. We first discuss in Section 3 the liquid nature of several artificial spin systems, and highlight the impact of the long range dipolar interaction coupling the nanomagnets on their low-energy properties. Section 4 focuses on one particular class of spin liquids: the Coulombic spin liquid. The purpose of this section is to show that such a phase, and its associated monopole-like excitations, can be imaged and studied in a properly designed artificial square system. We then turn to another class of spin liquids which has been introduced recently in condensed matter: the fragmented spin liquid. The aim of this Section 5 is to highlight how artificial spin systems provide a platform to observe these liquids both in real and reciprocal space. Finally, we discuss in Section 6 several possible directions for future work in the field.

2 Probing at- or out-of-equilibrium physics?

Artificial spin systems offer the appealing opportunity to image arrested magnetic configurations, in which the magnetic moments are resolved individually. A single snapshot of such an arrested magnetic state potentially allows capturing the many-body physics of frustrated spin systems by providing local and global information at the same time. But this imaging capability comes at a price: the artificial spin system under investigation has no dynamics, or this dynamics must be slow enough to be compatible with the typical acquisition time of the imaging technique. In other words, although the driving idea behind the study of artificial frustrated spin systems is to explore the physics of highly degenerate phases, and thus highly fluctuating magnetic configurations, artificial spin systems are essentially imaged in a frozen state (although they are a few exceptions, see Sect. 6).

We might then wonder whether the imaged frozen configurations are representative of a physics at thermodynamic equilibrium, or if instead out-of-equilibrium phenomena must be invoked. As one investigates frustrated spin systems for their exotic low-energy physics, one might wish these magnetic configurations to be representative of what is predicted by a spin model at thermodynamic equilibrium. This brings the question of how to prepare artificial frustrated spin systems so that they do not get trapped into trivial states, and how the resulting arrested magnetic configuration can be analyzed to highlight collective phenomena.

In this section, we discuss the relevance of confronting a single (or a limited number of) arrested magnetic configuration(s) to predictions from frustrated spin models describing highly fluctuating systems at thermodynamic equilibrium.

2.1 Shaking artificial spin systems

Bringing artificial spin systems into their ground state or within a low-energy manifold has been one of the first challenges the community faced after the pioneering works of Tanaka et al. [16,17] and Wang et al. [18]. Most of the time, one is interested in imaging correlated disorder or complex magnetic ordering. As mentioned above, the artificial spin system under investigation must be frozen, or only slowly fluctuating, to take a snapshot of a given configuration. Strategies must then be used to prepare the system into a nontrivial configuration, and to bring it into a low-energy manifold, where exotic behavior and many-body physics emerge.

So far, two main directions have been followed. The method initially proposed for athermal systems consists in applying a field demagnetization protocol, i.e., to cycle an external magnetic field in such a way that the overall magnetization of the sample is reduced down to the lowest possible value. Doing so, one then implicitly assumes that the ground state and low-energy configurations of the system are characterized by a small, possibly zero, magnetization (which is indeed often the case). The way the field might be ramped down during the demagnetization protocol has been discussed in several works [33–39] (see Fig. 2a). One interesting result is that frustrated spin systems, whether they are characterized by an ordered or a disordered ground state, continue to relax, even after the global magnetization has been minimized [35]. In particular, if the overall magnetization rapidly goes to low residual values, pairwise spin correlations further evolve as nanomagnets are given more chance to flip (see Figs. 2b and 2c). One possible interpretation is that the energy landscape in frustrated spin systems becomes rather flat once the global magnetization is low, and exploring the configuration space while minimizing the system energy requires a large amount of spin flip attempts. Another intrinsic and fundamental reason is that collective spin flip events are usually required to bring magnetic systems into their ground state. This is even the case in unfrustrated spin models. For example, if one tries to demagnetize an artificial realization of an Ising ferromagnet on a square lattice, we would likely end up with an arrested configuration showing large patches of the ordered ground state, i.e., large clusters of spins pointing ‘up’ and large clusters of spins pointing ‘down’, separated by domain walls. Unwinding and removing these domain walls is statistically unlikely in a large system with only a single spin flip dynamics. To make the system bifurcate, one would need experimentally to induce the reversal of entire clusters (i.e., global spin updates) [40–42], like this is done in numerical simulations. However, the spin dynamics in artificial spin systems cannot be collective, and a large number of single spin flip attempts is necessary to affect pairwise spin correlations, even after the overall magnetization has been minimized.

One might also wonder why a given field demagnetization protocol, which is intrinsically a deterministic process, allows reaching different, essentially uncorrelated, disordered states when applied several times to an artificial spin lattice. In other words, one could wonder what is the origin of the stochasticity observed experimentally when comparing consecutive, and almost identical, field demagnetization protocols applied to the very same array of nanomagnets. One reason that can be invoked is the non-ideal character of lithographically-patterned arrays of nanomagnets, which can be modeled by a distribution of magnetic properties. In particular, quenched disorder, either induced by a distribution of switching fields to reverse magnetization in each individual nanomagnet [43] or by a distribution of coupling strengths between neighboring elements, was shown to play a key role in bringing artificial spin systems into low-energy configurations [44–47]. The source of stochasticity might also be related to different types of magnetic ‘noises’ present

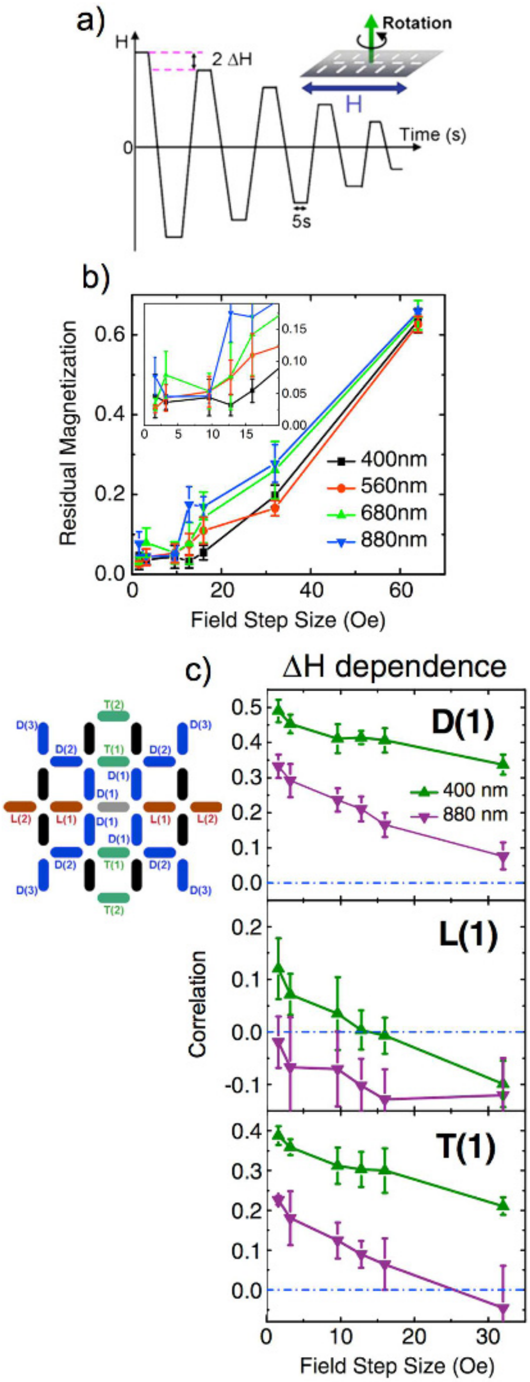

Fig. 2. (a) Time dependence of the external applied magnetic field used to demagnetize several artificial square spin lattices. The field direction is set within the lattice plane and the sample is put in rotation. As shown in the other panels, the important parameter in the demagnetization protocol is the field step size ΔH. (b) Residual magnetization of the square arrays after several field demagnetization protocols. As the field step size ΔH is reduced, residual magnetization becomes smaller, until it reaches a low value for step sizes of the order of 10 Oe or smaller. (c) Dependence of the spin–spin correlations with ΔH. Even when $\Delta H < 10$ Oe, correlations continue to evolve. The D(1), L(1) and T(1) notations for the spin–spin correlations are illustrated in the top-left sketch of the lattice (from Ref. [35] © 2008 the American Physical Society).

experimentally (non-ideal character of the magnetic field supplied by an electromagnet or role of temperature to trigger magnetization reversal).

Later on, artificial spin systems were made thermally active, either by reducing the volume of the individual magnetic nanostructures to adjust their blocking temperature [48–58] or by cooling/heating the system through the Curie temperature (T_C) of the constituent material [59–70]. These two approaches are of course not equivalent. Going through the Curie point implies that the constituent material loses ferromagnetism above T_C, and the whole system is getting remagnetized below T_C. Magnetic interactions between nanomagnets thus vary during the process, both in amplitude (interactions are proportional to the magnetic moments, which is a temperature-dependent quantity), and likely in direction as well (the nanomagnets are probably not Ising-like pseudo-spins close to T_C). In addition, because of the quenched disorder, the whole array does not instantaneously remagnetize everywhere, but more likely through a spin by spin process [67]. On the contrary, working close to the blocking temperature of the nanomagnets allows the entire system to thermally fluctuate, while keeping the magnetic moment and Ising character of the elements essentially unchanged.

Field demagnetization and thermal protocols seem to be equivalently efficient to reach low-energy configurations. They also share similar limitations. When the spin system orders, these protocols usually allow reaching magnetic states characterized by large patches of the ground state configuration. This is the case for instance in the artificial square spin system (see Sect. 3.5), in which large patches of the antiferromagnetic ground state ordering are found, regardless the protocol used. For degenerate systems, all strategies are unable to bring the array into a (very) low-energy manifold, although they permitted visualization of collective phenomena, such as the fragmentation of magnetism in the kagome dipolar spin ice (see Sect. 5.3). As mentioned above, this is so because the relevant (stochastic) spin dynamics then involves collective spin flip events, like loop or cluster moves. However, it is important to understand that only single spin flip events are accessible experimentally, at least in the systems used so far, whether the system is field demagnetized or thermally activated. Disordered artificial systems thus suffer from the critical slowing down of the single spin flip dynamics, prohibiting, intrinsically, access to low-energy magnetic states. This is a crucial point as the systems we are interested in and which exhibit collective and exotic phenomena become loop models [71][1] in their low-temperature regime (see Sects. 4 and 5). Otherwise said, the sad news is that exploring these loop models experimentally, with the current approach provided by artificial spin systems (or even in bulk compounds), is a lost battle. What saves us is that these collective and exotic phenomena are nevertheless partially accessible, mainly because of the finite size of the studied artificial systems. Fingerprints and signatures of the many-body physics associated with frustrated spin systems can then be captured, provided that these systems are efficiently demagnetized based on a single spin flip dynamics.

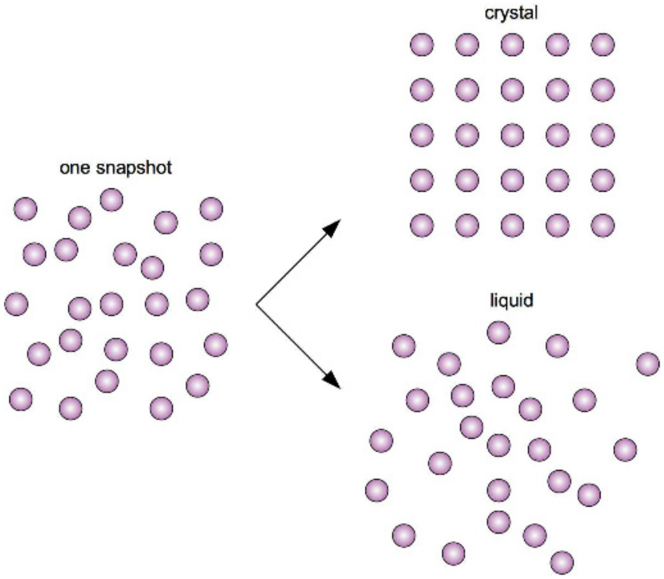

Fig. 3. Schematics illustrating the atom positions in an arrested configuration obtained at finite temperature in a hypothetical pure element. The question is whether the snapshot on the left is evolving towards a crystal if the temperature could be further reduced, or if it would evolve towards a liquid state.

2.2 Statistical analysis of an arrested magnetic configuration

One of the main challenges usually faced with artificial spin systems is the low statistics available with imaging techniques compared to macroscopic measurements, such as magnetization, susceptibility or neutron scattering experiments generally employed when studying bulk compounds. Most of the time with artificial systems, one is left with one, or only a few, static magnetic images of a limited number of elements, while the ultimate goal is to explore collective phenomena. For example, spin liquids are often described as highly fluctuating magnetic systems with a spin dynamics persisting down to very low temperatures. The question then arises of whether artificial spin systems can be considered as spin liquids although dynamical imaging is in practice complex to achieve, except to image very slow dynamical processes (see for instance Ref. [53]).

This intrinsic difficulty can be illustrated through a simple analogy. Considering a snapshot of atom positions like schematized in Figure 3, the question we want to answer is whether this snapshot represents:

---

[1] Loop models, as those described in [71], are defined by one-dimensional degrees of freedom, which thermodynamics is driven by their statistical weights in the partition function. In spin models, as the ones discussed in this work, loops actually correspond to a closed head-to-tail arrangement of Ising spins. For example, in the low-energy square ice manifold, spin fluctuations are energetically prohibited as the ice rule is enforced. Nevertheless, fluctuations are possible, provided that they correspond to *global* fluctuations preserving the ice rule constraint (see Sect. 4.1). Loop moves correspond to such fluctuations, hence the correspondence, or mapping, between spin ice models and loop models at low temperatures, i.e. within the ice manifolds.

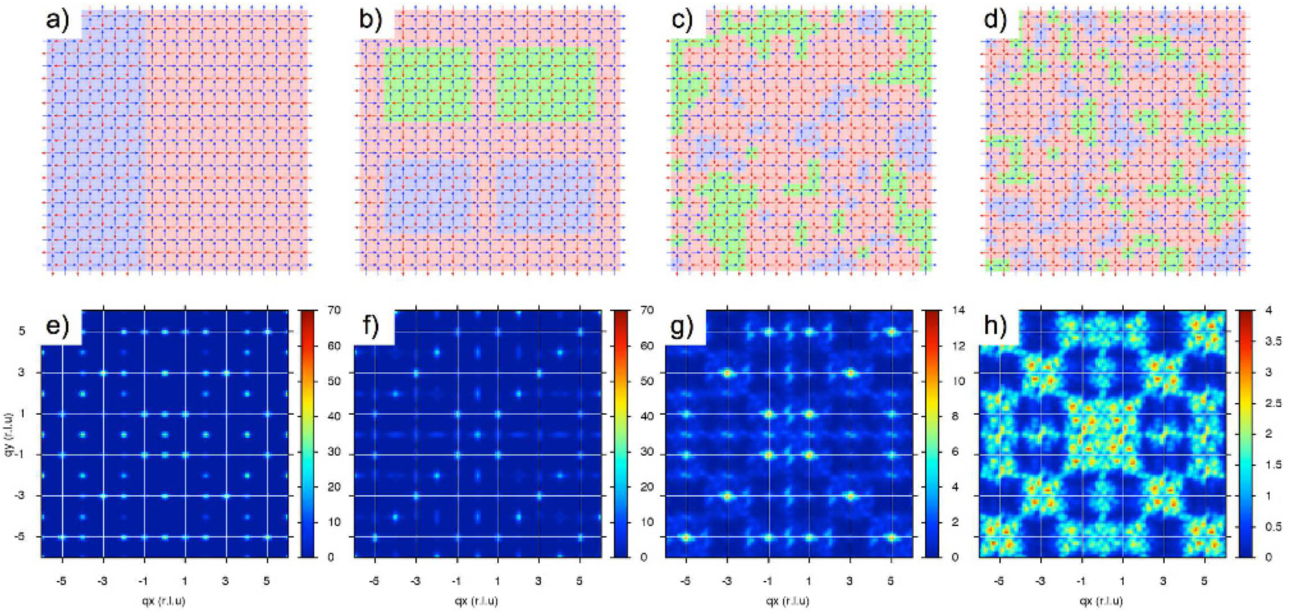

Fig. 4. Magnetic configurations (a–d) and their associated magnetic structure factors (e–h) for a square spin system. (a–d) Red and blue arrows represent the local spin direction. The red, blue and green squares represent the local vertex configuration. Blue and green squares are associated with type I vertices, while red squares are associated with type II vertices. In these four magnetic configurations, the populations of type I and type II vertices are similar: (a) 38%/62%, (b) 41%/59%, (c) 38%/62% and (d) 38%/62%, respectively. But obviously, they show distinct properties. (e–h) Magnetic structure factors reveal clear magnetic Bragg peaks in the three first cases (e–g), while it shows in the last case (h) a diffuse signal characteristic of a spin liquid state.

- an arrested state of a crystal held at high temperature so that atom positions are not well-defined;
- a liquid, in which atom positions develop spatial correlations;
- or a random distribution of particles, typical of an ideal gas.

Increasing significantly the size of this image or, equivalently, increasing the number of snapshots, would obviously help characterizing the nature of the ordered or disordered state involved. But answering this question can be more challenging if only a few static snapshots, with a limited number of particules, are available.

From a magnetic image, where each individual spin configuration $\boldsymbol{S}_i$ is measured unambiguously, several quantities can be estimated. For instance, the total magnetic moment $\boldsymbol{M}$ of a given state can be easily determined as $\boldsymbol{M} = \sum_i \boldsymbol{S}_i$. A second natural quantity that comes to mind is the counting of the vertex populations. This is particularly useful when the system is characterized by a magnetically ordered ground state. In that case, vertex populations give a good flavor of how far the system is from perfect ordering. If one assumes that the interactions are only between nearest neighbors, then the system energy is simply the sum of all individual vertex energies, and the estimate of the vertex populations is a direct measure of the system energy. Counting the vertex populations can also be interesting for understanding to what extent certain constraints induced by the frustration are obeyed in the array. However, this type of analysis quickly shows strong limitations. First, as we will see below, artificial spin systems are dipolar by nature and considering only interactions between nearest neighbors is a crude approximation. Second, this type of analysis is essentially useful for trivial ground state ordering but does not always provide meaningful information to characterize a disordered state.

Looking at the square spin system is instructive, although the same arguments apply for other geometries. In the quest of the degeneracy in the square ice model (see Sects. 3.5 and 4), one expects to have about 33% of type I vertices and about 67% of type II vertices (see Sect. 3.5 for the definition of the vertex types in the square ice) and zero net magnetization, at thermodynamic equilibrium. However, measuring the magnetization or the vertex populations does not tell anything about the spatial distribution of these two vertex populations. One can imagine very different states with ordered or disordered patches of type I and type II vertices such that their populations are 33% and 67% (see Fig. 4). Comparing Figures 4a–4d, one immediately sees that these two population values alone do not tell much about the magnetic state of the system. If these examples are obvious illustrations that magnetization and vertex populations are not good quantities to describe a disordered state, there might be more subtle cases where this demonstration is not as trivial. For example, Figures 4c and 4d show two fairly similar magnetic configurations, not only in terms of vertex populations, but, to a certain extent, also in terms of spatial arrangement of these vertices. At first glance, seeing that the physics at play is drastically different in these two cases might be challenging.

This difference is however clearly seen after performing a Fourier transform of the pairwise spin correlations deduced from the real space configurations. Such a Fourier analysis provides the so-called magnetic structure factor, i.e., the magnetic diffraction pattern associated with the considered real space magnetic state (see Figs. 4e–4h). Comparison between Figures 4c and 4d, not in real space but in reciprocal space, is now striking: one shows magnetic Bragg peaks, while the other is characterized by a diffuse, but structured, background signal (see Figs. 4g and 4h). In the former case (Figs. 4c and 4g), the magnetic configuration shows clear tendency to ordering, while in the latter (Figs. 4d and 4h), the magnetic snapshot ressembles a spin liquid state. Being able to characterize a disordered state then often requires to analyze the magnetic correlations that develop in the array. Since artificial spin systems provide real space images of magnetic configurations, pairwise spin correlations can be measured and averaged over the entire array or estimated locally. Besides their interest to characterize magnetic order or disorder, they provide a set of useful data that can be directly confronted to model predictions. They can be used for instance to test the relevance of different spin models to capture the physics at play (see Sect. 3) and to determine if a given configuration is representative of a physics at thermodynamic equilibrium or of an out-of-equilibrium physics (see following Sect. 2.3).

2.3 Comparison with thermodynamics

The set of measurements providing the values of the residual magnetization, of the vertex populations and of the spin–spin correlations can be confronted to predictions from various spin models. Indeed, one might want to know if the arrested configurations that have been imaged can be described by a physics at thermodynamic equilibrium or if an out-of-equilibrium physics is present. Once an artificial spin system has been demagnetized, understanding whether this system has been quenched or brought to a magnetic configuration representative of a manifold at thermodynamic equilibrium is of crucial importance to identify the relevant scientific framework describing the observed phenomena. As a matter of fact, this question comes together with the choice of a spin Hamiltonian. As we will see below, the physics at work in artificial spin systems is most of the times a physics at thermodynamic equilibrium, and the proper choice of the Hamiltonian is a spin Hamiltonian that includes long range dipolar interactions.

The claim that the physics of artificial spin systems is well-described by the equilibrium statistical mechanics of a dipolar spin Hamiltonian might sound trivial at first sight. But considering that the nanomagnets used experimentally:

– are not point-dipoles (their typical length is of the order of the lattice constant);

– are not macrospin objects (their behavior is described by micromagnetism, and magnetization reversal within a given nanomagnet involves the nucleation and propagation of magnetic domain walls);

– and do not behave like pure Ising-like variables (the magnetization distribution within a nanomagnet is not uniform because of its micromagnetic character), it is in fact quite a miracle that a simple Ising spin model on a lattice captures most of the physics observed experimentally. Furthermore, because artificial spin systems are never defect-free and are often shaken using rough protocols (see Sect. 2.1), being capable of measuring signatures of the long range dipolar interaction coupling the nanomagnets, within a single snapshot of an equilibrated magnetic configuration is also quite astonishing. Otherwise said, the whole complexity and high degree of imperfection of a two-dimensional arrangement of magnetic nanostructures can be encompassed by a spin Hamiltonian of the form $\sum_{(i,j)} J_{ij}\ \sigma_i\sigma_j$, where σ is an Ising variable and J_{ij} is the interaction strength that couples two point dipoles. It is worth noting that including long range coupling terms in the spin Hamiltonian is not simply a matter of how accurate is the description of a given magnetic configuration. In some cases, the short range and dipolar spin Hamiltonians have very distinct low-temperature behaviors (see Sects. 3.2 and 3.3), although they are very often not distinguishable in their high temperature regime. In particular, the richness of the many-body physics in the kagome lattice is intimately related to the dipolar nature of the interaction coupling the nanomagnets (see Sect. 5).

One important consequence of identifying the physics at play is the possibility to associate an (fictional) effective temperature to a given magnetic microstate imaged experimentally [39,72]. Intrinsically, this effective temperature does not represent much as artificial spin systems are essentially athermal systems. For example, this effective temperature does not provide any information on how the system actually fluctuates or gets frozen. However, it does provide key information to evidence collective phenomena. If artificial spin systems can be modeled by a dipolar spin Hamiltonian and a physics at thermodynamic equilibrium, the properties of a given arrested state are then known completely. In particular, the average values and associated standard deviations of quantities, such as magnetization, vertex populations, pairwise spin correlations, energy, etc., are now determined at any temperature. This effective temperature is thus interesting as it allows to say that a given snapshot is characteristic (or not) of an ordered or a disordered state at thermodynamic equilibrium.

In fact, the comparison between the experimental and theoretical pairwise spin correlation coefficients is sensitive enough to detect deviations from the predictions of an at-equilibrium physics. This can be seen for example in a thermally active artificial kagome dipolar spin ice [67]. The spin–spin correlations $C_{\alpha j}$ for the seven first neighbors have been calculated for all temperatures using Monte Carlo simulations (see Fig. 5). These spin correlators are represented by different colors and greek symbols. The nearest-neighbor coefficient $C_{\alpha\beta}$ is represented in black, while the two nonequivalent third neighbors ($C_{\alpha\nu}$ and $C_{\alpha\delta}$) are shown in green and light blue, respectively. At high temperature, the system is paramagnetic and all spin–spin correlation coefficients equal zero on average. As the temperature is reduced, correlations start to develop and the system encounters

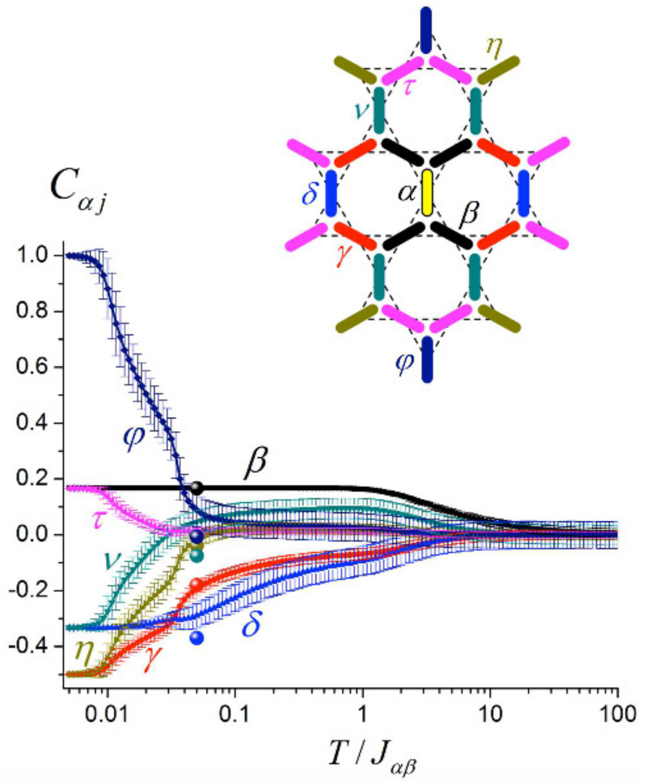

Fig. 5. Pairwise spin correlations $C_{\alpha j}$ as a function of temperature T (normalized to the coupling strength $J_{\alpha\beta}$ between nearest-neighbor elements). The curves are deduced from Monte Carlo simulations using a kagome dipolar spin ice Hamiltonian. The dots are experimental measurements. Different colors are used to distinguish spin–spin correlators, as schematized in the inset. All seven experimental values (dots) fall on the Monte Carlo curves for a $T/J_{\alpha\beta}$ temperature of the order of 0.05, although the $C_{\alpha\delta}$ and $C_{\alpha\nu}$ correlators deviate substantially from their corresponding Monte Carlo predictions. These deviations are attributed to kinetic effects during the thermal annealing of the experimental array (from Ref. [67] © 2014 the American Physical Society).

several phase transitions (see Sect. 3.3). In this figure, the experimental values deduced from a set of magnetic images are represented as colored dots. With a good approximation, these seven dots fall on the predicted curves for a temperature of about 5% of the coupling strength $J_{\alpha\beta}$ between nearest neighbors. However, the $C_{\alpha\nu}$ and $C_{\alpha\delta}$ spin correlators slightly deviate from these predictions. $C_{\alpha\delta}$ even reaches a value that is not in the range of possible values predicted by the Monte Carlo simulations. These differences can be accounted for by including some kinetic effects during the (de)magnetization process [67]. We emphasize here again that analyzing the residual magnetization or the vertex populations cannot usually provide such a fine description of the system, while correlations are powerful quantities that were used to prove that the physics is dipolar and not short ranged, and that out-of-equilibrium physics can be even detected in specific cases.

3 Artificial spin liquids

One of the initial motivations of fabricating artificial spin systems was to access, directly in real space, the physics of disordered magnetic states, such as spin liquids. More generally, artificial spin systems offer the promise of being capable to image, spin by spin, collective states of matter and cooperative magnetic phenomena, thus allowing to probe, at the desired length scale, the complex many-body physics of frustrated spin systems. The main purpose of this section is to discuss to what extent artificial spin systems behave as spin liquids, and after recalling what we mean by spin liquid, the properties of several systems will be reviewed. We leave aside for now other collective phenomena that will be introduced and presented in the following sections.

One important point we want to stress in this section is that, by design, artificial spin systems are dipolar. The associated spin models used to capture their thermodynamic properties are thus long ranged, and this is not a small detail. For example, in the kagome spin ice, the dipolar interaction leads to new collective phenomena, such as charge crystallization, spin fragmentation and Coulomb phase physics (see Sects. 4 and 5) that are simply absent in the short range version of the very same model. Experimentally, signatures of all these three phenomena are found, indicating that dipolar interactions drive the (low-temperature) physics of artificial spin systems. From our point of view, it is precisely the long range nature of the magnetostatic interaction coupling the nanomagnets that makes the physics of artificial spin systems rich and interesting. Attention will then be paid in this section to illustrate the impact of the dipolar interaction on the liquid behavior of several artificial spin systems studied these last few years.

3.1 What is an artificial spin liquid?

Before describing the physics of spin liquid state(s), we define here what we mean by artificial spin liquid. The motivation of this subsection is twofold. First, although the concept of spin liquid is not new and relatively well understood, at least for classical spin systems, finding a simple, well-admitted and general definition is in fact a difficult task [73–75]. Second, new concepts, such as the magnetic moment fragmentation [76], emerged recently, extending the idea of spin liquids to fragmented spin liquids [77], characterized by their own dynamics and exotic properties (see Sect. 5).

First of all, throughout the paper, we limit our discussion to classical spin systems as no quantum effects are expected in assemblies of nanomagnets as those we usually consider in artificial spin systems. Moreover, in all systems studied so far, spins have an Ising character, meaning that continuous degrees of rotation as those found in XY or Heisenberg models are not considered. Within this (very) restricted framework, by artificial spin liquid, we mean a disordered but correlated magnetic state, built from an assembly of classical interacting Ising variables, in which pairwise spin correlations are not zero, but decay to zero at large distances.

However, it must be pointed out that the term liquid might be confusing and is mainly intended to draw an analogy with the three conventional states of matter (solid, liquid and gas) [73]. In particular, if one can reasonably compare a paramagnet to a gas (i.e., an uncorrelated disordered state at high temperature), and a ferromagnet (or an antiferromagnet) to a crystal (i.e., a long range ordered state at low temperature), the concept of spin liquid is more subtle in many aspects. First, contrary to the three conventional states of matter, certain spin liquids remain disordered even at the lowest possible temperature, while some other spin liquids do crystallize when reducing the temperature. For example, the kagome Ising (kI) antiferromagnet remains fluid at any temperature (see Refs. [78–80] and Sect. 3.2 below), while the kagome dipolar spin ice is characterized by a well-defined long range order (LRO) at low temperature [81,82]. Second, whereas classical liquids have only local correlations, some classical spin liquids can be characterized by a correlation length that diverges and pairwise spin correlations that are long ranged. These properties are not intuitive and make spin liquids different from conventional liquids.

In fact, two types of classical spin liquids are usually studied. The first one is often called a cooperative paramagnet [83], has a finite correlation length (of the order of one lattice constant) and spin–spin correlations that decay exponentially with the distance. The kI antiferromagnet (or equivalently the short range kagome spin ice) described below is an example of a cooperative paramagnet. The second one, although also a cooperative paramagnet, is often called an algebraic spin liquid as the pairwise spin correlations have a power-law dependence and an *infinite* correlation length. This is the case for example of the spin ice II phase present in the kagome dipolar spin ice (see Refs. [81,82] and Sect. 3.3).

3.2 The kagome Ising antiferromagnet

The triangular and kagome Ising (kI) antiferromagnets, together with the square ice, are probably the first studied classical spin liquids in two dimensions [78–80,84,85]. The kI antiferromagnet consists of a kagome lattice on which Ising spins are located, their anisotropy axis being perpendicular to the kagome plane (see Fig. 6a). In this model, spins interact antiferromagnetically, between nearest neighbors only. The corresponding spin Hamiltonian H can then be written as:

$$H = -J \sum_{<ij>} \boldsymbol{S}_i \cdot \boldsymbol{S}_j \tag{1}$$

where J is negative and defines the coupling strength between the spins $\boldsymbol{S}_i$ and $\boldsymbol{S}_j$ residing on the sites i and j, respectively. In this expression, $<ij>$ means that the summation is made over nearest neighboring spins. Because each spin points along the direction perpendicular to the kagome plane, the Hamiltonian can take a scalar form:

$$H = -J \sum_{<ij>} \sigma_i \sigma_j \tag{2}$$

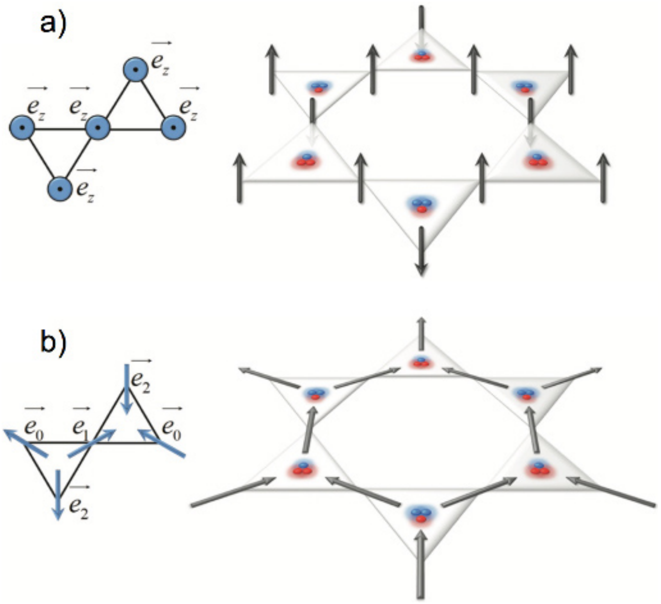

Fig. 6. Schematics of the kagome Ising (kI) antiferromagnet (a) and kagome spin ice (b). The grey arrows represent the spin direction: spins are pointing along the angle bisectors in the kagome spin ice, while they all point out of the kagome plane in the kI antiferromagnet. The blue and red clouds at the vertex sites correspond to the magnetic charges associated with the spins, when these spins are described using a dumbbell charge picture. In the kagome spin ice, a red/blue cloud (+1/ − 1 magnetic charge) is associated to the head/tail of an arrow. In the kI antiferromagnet, a red/blue cloud (+1/1 magnetic charge) is associated to the head/tail of an arrow for a Δ triangle, while the opposite convention is used for a ∇ triangle to ensure charge neutrality. The unit vectors $\boldsymbol{e_i}$ used to define the spin directions are represented by blue arrows on the left (from Ref. [92] © 2014 the American Physical Society).

with $\boldsymbol{S}_i = \sigma_i \boldsymbol{e}_z$, where $\boldsymbol{e}_z$ is a unit vector normal to the lattice plane, while σ_i is a scalar giving the spin's orientation along this direction (+1 if parallel to $\boldsymbol{e}_z$ and −1 otherwise). The fact that $\sigma_i = \pm 1$ ensures that the spins are Ising variables.

The thermodynamics of this model is described by two temperature regimes separated by a crossover (there is no phase transition) [79,80]. At high temperature, i.e., when $T/J \gg 1$, the system is in a paramagnetic state and all types of local configurations are allowed on a given triangle of the kagome lattice (all eight configurations illustrated in Fig. 1a are accessible). As the temperature is reduced, short range correlations start to develop, eliminating the two local configurations with the three spins pointing in the same direction. When $T/J \ll 1$, the system is in a cooperative paramagnet state. This name comes from the fact that the system is highly fluctuating, in the manner of a paramagnet [83], although every triangular unit cell of the kagome lattice must obey the so-called (kagome) ice rule [86,87]: a local configuration can be only one of the six low-energy arrangements reported in Figure 1a. Otherwise said, the system is characterized by a magnetic susceptibility that varies like $1/T$ down to the lowest possible temperatures [88]. This low-temperature

Table 1. Theoretical values (deduced from Monte Carlo simulations) of the pairwise spin correlation coefficients C_{ij} in the low-temperature manifold of the kagome spin ice and kagome Ising antiferromagnet [39,92]. Note that these correlations are temperature independent once the system entered the spin ice manifold.

C_{ij}	$\alpha\beta$	$\alpha\gamma$	$\alpha\nu$	$\alpha\delta$	$\alpha\tau$	$\alpha\eta$	$\alpha\phi$
n^{ith}	1	2	3	3	4	5	6
Spin ice	0.167	−0.062	0.101	−0.075	0.012	0.019	0.023
Ising AF	−0.333	0.124	0.101	−0.075	−0.024	−0.038	0.023

phase is often referred to as a spin liquid state, characterized in that case by a macroscopically degenerate ground state manifold (the entropy per site is 0.501) and pairwise spin correlations that decay exponentially with the distance [89].

This short range kI antiferromagnet model can be mapped, one to one, onto a short range kagome multiaxis Ising ferromagnet model (kagome spin ice), where geometrical frustration is provided by in-plane Ising-like anisotropies [90,91] (see Fig. 6b). The corresponding spin Hamiltonian H can be written as:

$$H = -J \sum_{<ij>} \boldsymbol{S}_i \cdot \boldsymbol{S}_j \tag{3}$$

where J is now positive. Because the spins point along the bisectors of the equilateral triangles making the kagome lattice, this Hamiltonian can also take a scalar form:

$$H = -J \sum_{<ij>} \sigma_i \sigma_j \; \boldsymbol{e}_i \cdot \boldsymbol{e}_j = +\frac{J}{2} \sum_{<ij>} \sigma_i \sigma_j \tag{4}$$

with $\boldsymbol{S}_i = \sigma_i \boldsymbol{e}_i$, where $\boldsymbol{e}_i$ is a unit vector that now defines the local anisotropy direction. It is important to note that the two Hamiltonians reported in equations (2) and (4) differ only by a factor $-1/2$. In other words, the two models are identical: they are both described by two temperature regimes, including a macroscopically degenerate ground state manifold, and they must develop identical exponentially decaying pairwise spin correlations in their low-temperature spin liquid regime. The values of the first seven spin–spin correlations are given in Table 1 for the two models.

We emphasize that these two models are identical if nearest-neighbor interactions only are considered. This equivalence is of course not valid anymore if long range dipolar interactions are taken into account. In particular, while in the kI antiferromagnet all spin–spin interactions favor an antiferromagnetic alignment of the spins for all distances, in the kagome spin ice, these interactions lead to a ferromagnetic or antiferromagnetic coupling depending on the considered pair of spins. Adding long range dipolar interactions to these models, one then expects their low-temperature behavior to be modified and distinct. We will see below that the analysis of the spin–spin correlations measured experimentally indeed confirms that each artificial system has its own story to tell [92].

3.3 The artificial kagome dipolar spin ice

We mentioned above that the kI antiferromagnet and the kagome spin ice (see Fig. 6) are expected to develop distinct low-temperature behaviors when long range, dipolar interactions couple the spins. We address here the physics of the kagome dipolar spin ice, and show how the corresponding phase diagram differs form the cooperative paramagnet described in Section 3.2. For the sake of completeness, the spin Hamiltonian we consider in this section can be written as:

$$H = -\frac{D}{2} \sum_{(i,j)} \left[\frac{3(\boldsymbol{S_i} \cdot \boldsymbol{r}_{ij})(\boldsymbol{S_j} \cdot \boldsymbol{r}_{ij})}{r_{ij}^5} - \frac{\boldsymbol{S_i} \cdot \boldsymbol{S_j}}{r_{ij}^3} \right] \tag{5}$$

where D is the dipolar constant.

The kagome spin ice was the first geometrically frustrated system studied via an array of interacting nanomagnets [16]. The pioneering work of Tanaka et al. revealed that such artificial kagome arrays have clear tendency to select local configurations satisfying the (kagome) ice rule constraint [86,87]. Comparing the magnetic configurations obtained experimentally with predictions from Monte Carlo simulations of the nearest-neighbor kagome spin ice [89], Qi et al. went a step further and demonstrated that the observed ice-like physics in arrays of nanomagnets could not be described solely by a short range spin Hamiltonian [93]. In fact, the analysis of the pairwise spin correlations deduced from the real space magnetic images revealed substantial discrepancies compared to the values derived from Monte Carlo simulations [89], especially for the second ($C_{\alpha\gamma}$) and third ($C_{\alpha\delta}$) neighbors. This work is important as it shows that dipolar interactions lead experimentally to a low-temperature physics that differs from the one of the kI antiferromagnet. This result has been later confirmed unambiguously through the analysis of spin–spin correlations up to the seventh neighbors [39].

The fact that an array of nanomagnets coupled through magnetostatics behave as a dipolar spin system and not as a short range spin system might sound trivial. However, it was first not obvious whether or not signatures of the dipolar interactions could be detected experimentally. For example, the intrinsic disorder present in any experimental array could have screened completely the dipolar interactions, and the imaged magnetic disorder could have been dominated by local defects. In addition, the finite length of the nanomagnets and the short edge-to-edge distance between neighboring elements compared to the lattice constant could have strongly reduced the impact of the dipolar coupling strength. And finally, since the short range (Eq. 4) and the long range (Eq. 5) versions of the same Hamiltonian are hardly distinguishable in their high temperature regimes [39], dipolar interactions could have been neglected (and as a matter of fact, they were first neglected) simply because of the technical difficulty to bring an artificial spin system into its low-energy manifold. In short, although the physics looks like short range at first sight, the artificial kagome spin ice, and more generally artificial spin systems based on arrays of nanomagnets are dipolar.

The first consequence is that the phase diagram of the dipolar kagome ice is much richer and way more exotic than the kI antiferromagnet described in Section 3.2. More specifically, Monte Carlo simulations of the kagome dipolar spin ice reveal a two stage ordering process at low temperatures (see Fig. 7a) [81,82]. The system first exhibits a crossover from a high temperature paramagnetic phase (i.e., when $T/J \gg 1$) to a first spin liquid phase when $T/J \sim 1$, J being the nearest neighbor coupling strength. This liquid phase is often referred to as the spin ice I phase in the literature. Similar to the kI antiferromagnet described in the previous section, there is no phase transition and the system strongly fluctuates with an additional constraint associated with the so-called kagome ice rule. As the temperature is reduced, longer range couplings further correlate the system, which undergoes a first phase transition towards a second spin liquid phase (refereed to as the spin ice II phase). Most of the residual entropy is released, but not all of it (see Fig. 7a), meaning that the phase is still macroscopically degenerate [81,82]. Besides the ice rule constraint, this second spin liquid phase has an additional constraint: spins are allowed to fluctuate if they satisfy both the ice rule and the formation of a magnetic charge crystal, given the dumbbell charge description of the magnetic moment [81,82,94]. Eventually, a second phase transition occurs at the lowest temperatures and a LRO sets in (see Fig. 7b).

We emphasize that the spin ice I phase is not equivalent to the short range kagome spin ice (i.e., the kI antiferromagnet). In particular, the pairwise spin correlations are temperature dependent in the spin ice I phase, while they are constant in the short range kagome spin ice [39,92]. The two spin liquids thus differ in the sense that the spin ice I phase has continuously evolving spin–spin correlations as the temperature is reduced, meaning that all configurations satisfying the ice rule do not have the same energy, contrary to the spin manifold associated with the short range kagome ice.

One puzzling aspect of the spin ice II phase is the emergence of a hexagonal pattern of alternating +1 and −1 magnetic charges located at the vertices of the kagome lattice, on top of which spins can still highly fluctuate. This property is not only predicted numerically, but has been evidenced experimentally as well [39,55,62,65,67–69] (see Fig. 8). The intriguing aspect of this charge crystallization is that no charge degree of freedom is encoded in the underlying dipolar spin Hamiltonian (see Eq. 5), and the magnetic charge order somehow comes out of the blue. We will see in Section 5 that its existence has in fact deep roots in the associated dipolar spin model [69], but at this stage, the spin ice II phase can be regarded as a spin liquid that sits upon a magnetic charge crystal. Another intriguing property of this phase is the nature of the spin–spin correlations: while these correlations decay exponentially with the distance in the short range kagome ice, they decay algebraically in the kagome dipolar spin ice. This is also puzzling as algebraic spin liquids are usually associated to Coulomb phases (see Sect. 4), and characterized, *in spin ice systems*, by a divergence-free condition at the vertex sites, in sharp contrast with the charged vertices in the kagome lattice (see Sect. 5).

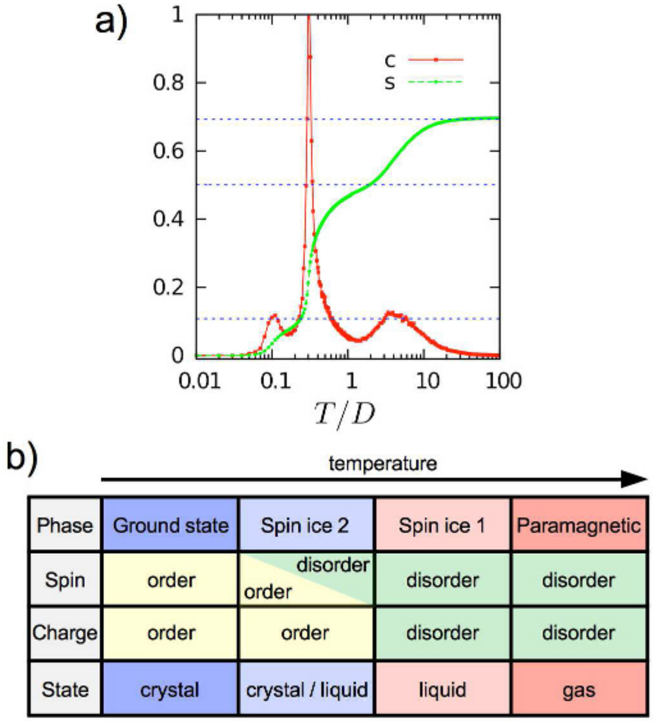

Phase	Ground state	Spin ice 2	Spin ice 1	Paramagnetic
Spin	order	disorder order	disorder	disorder
Charge	order	order	disorder	disorder
State	crystal	crystal / liquid	liquid	gas

Fig. 7. (a) Temperature dependence of the specific heat $c(T)$ (red curve) and entropy per spin $s(T)$ (green curve) for the kagome dipolar spin ice. The dashed blue lines show several levels of entropy per site: $s = 0.693$ (Ising paramagnet), 0.501 (spin ice I phase) and 0.108 (spin ice II phase) (from Ref. [82] © 2011 the American Physical Society). (b) Table illustrating the different magnetic phases in the kagome dipolar spin ice.

3.4 The artificial kagome dipolar Ising antiferromagnet

While the at-equilibrium and out-of-equilibrium properties of the artificial kagome dipolar spin ice have been extensively investigated, both numerically [81,82] and experimentally [39,55,62,65,67,68,93], much less is known on the thermodynamics of the artificial kagome dipolar Ising antiferromagnet. In particular, the nature of the spin liquid phase expected at low temperature and the properties of the ground state have been only partly addressed so far [92,95–97]. Many questions then remain open, for example regarding the number of phase transitions, the value of the residual entropy associated with the low-energy manifold and the relevant collective

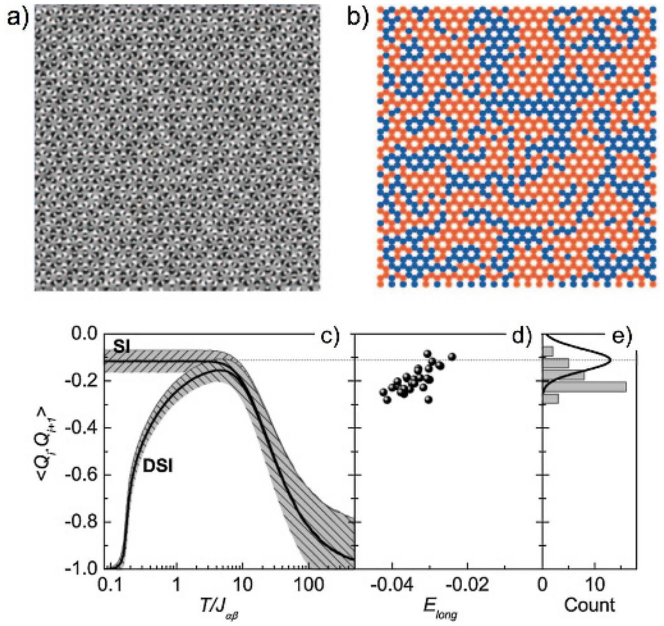

Fig. 8. (a,b) From reference [62] (Reprinted by permission from Springer Nature © 2013). Emergent magnetic charge domains in the artificial kagome dipolar spin ice. (a) Real space magnetic image of an arrested spin configuration. (b) Corresponding map of the magnetic charge distribution where the red and blue dots represent the two degenerate magnetic charge ordered states. (c–e) From reference [39] (© 2011 the American Physical Society). (c) Theoretical nearest neighbor charge-charge correlators (bold lines) and their standard deviations (hatched regions) calculated from the short range (SI) and dipolar (DSI) kagome spin ice models as a function of temperature. (d) Experimental values of the charge-charge correlators measured for 34 arrays of nanomagnets. (e) Histogram of the experimental charge-charge correlators compared to the nearly Gaussian distribution computed in the short range kagome spin ice model.

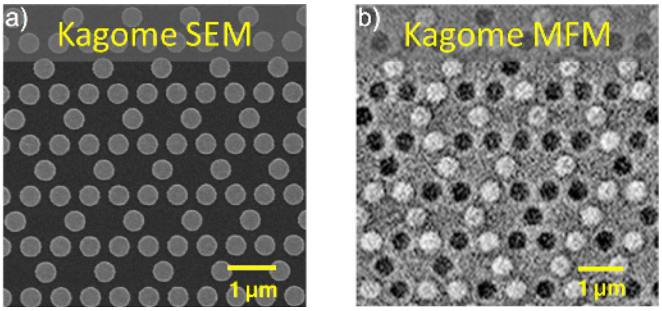

Fig. 9. Artificial arrays of ferromagnetic nanodisks with perpendicular magnetic anisotropy made to mimic the properties of the kagome Ising antiferromagnet. (a) Scanning electron micrograph of a portion of the array. The magnetic disks are located on the nodes of a kagome lattice. (b) Magnetic force microscopy image of the same lattice after a field demagnetization protocol. Black and white contrasts give the local direction of the out-of-plane magnetization (from Ref. [95] © 2012 the American Physical Society).

spin dynamics that needs to be activated to overcome the critical slowing down when approaching the ground state [98].[2]

Interestingly, the first investigations on the kagome dipolar Ising antiferromagnet were experimental and made through the magnetic imaging of lithographically patterned arrays of ferromagnetic nanodisks having out-of-plane magnetization [95] (see Fig. 9). At first glance, the analysis of the pairwise spin correlations obtained after an ac demagnetization protocol reveals striking similarities with those found for the kagome (dipolar) spin ice, suggesting a possible universality in artificial spin ice behavior [95]. Further experiments later showed clear limitations to this universality and permitted to understand the origin of the similarities [92]. Both models indeed develop similar pairwise spin correlations in their high temperature regime, just after the system starts to correlate upon cooling from the paramagnetic phase. However, longer ac demagnetization protocols, together with stronger inter-island interactions, successfully lower the effective temperature of the system and allow reaching a temperature regime where both systems develop distinct behaviors (see the predicted temperature dependence of the spin–spin correlators reported in Figs. 10a and 5 for the kagome dipolar Ising antiferromagnet and the kagome dipolar spin ice, respectively).

Another way to visualize these differences is to consider the nearest-neighbor charge-charge correlator rather than the pairwise spin correlations. As discussed in Section 3.3, the concept of magnetic charge has proven to be particularly useful to describe the two-stage ordering process present in the kagome dipolar spin ice [81,82]. Although less intuitive for the kagome dipolar Ising antiferromagnet, the very same definition of the magnetic charge can be used [92]. In particular, recalling that the short range versions of the kI antiferromagnet and kagome spin ice show identical physics (see Sect. 3.2), the temperature-dependence of their nearest-neighbor charge-charge correlations are also identical (see Fig. 8c, where $\langle Q_i Q_{i+1} \rangle = -1$ at high temperature and $-1/9$ in the spin liquid phase). However, when long range dipolar interactions are taken into account, the pairwise charge correlators show distinct trends and even have opposite signs (see Fig. 10b). The nearest-neighbor charge-charge correlator is thus a convenient quantity to distinguish experimentally the two physics, especially when demagnetization protocols hardly bring the corresponding artificial arrays into their low-energy manifold.

Monte Carlo simulations of the kI antiferromagnet also reveal that long range dipolar interactions drastically modify its low-temperature behavior [92]. More specifically, if the low-energy manifold is not known, the system seems to present a long range ordered ground state. A potential candidate for this ground state has been proposed [96] and consists of a rectangular crystal of a 12-spin magnetic unit cell, commensurable with the underlying triangular Bravais lattice, as reproduced in Figure 10c. This ground state candidate is also characterized by ferromagnetically charged stripes (Fig. 10d), in sharp contrast

---

[2] During the reviewing process, a new article appeared addressing some of these issues. We refer the reader to reference [98].

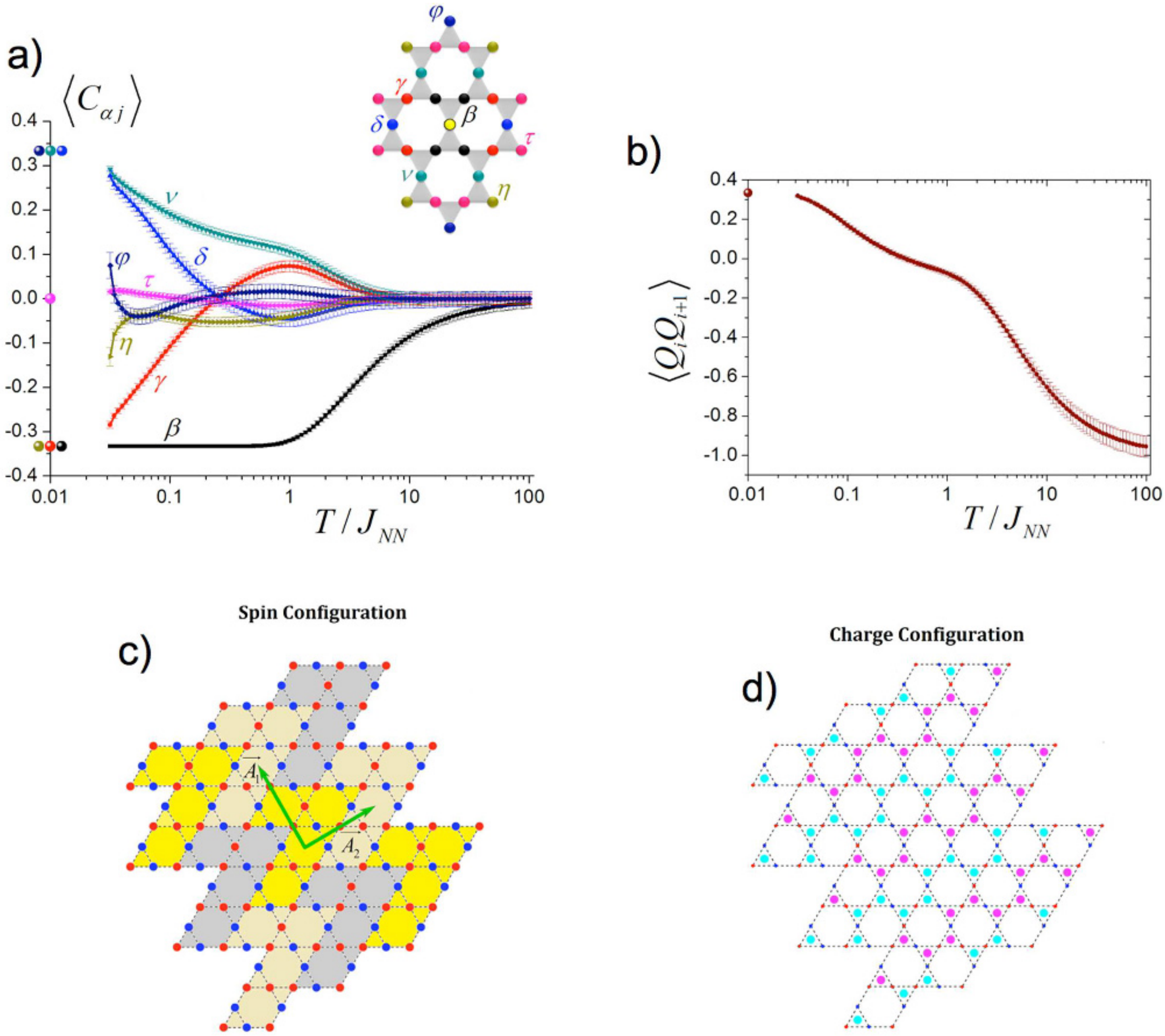

Fig. 10. Temperature dependence of the (a) pairwise spin correlations and (b) nearest-neighbor charge correlator. Inset in (a) gives the notations used to label the first seven spin–spin correlation coefficients. (c) The spin configuration of the ground state candidate is a crystal of 7-shaped unit cells with a rectangular basis ($\boldsymbol{A}_1, \boldsymbol{A}_2$). Each unit cell contains 12 spins, represented by red and blue dots corresponding to the 'up' and 'down' spin states, respectively. (d) Vertex magnetic charges, represented by magenta and cyan dots for the +1 and −1 charge states, respectively (from Ref. [96] © 2016 the American Physical Society).

with the antiferromagnetic charge crystal observed in the kagome dipolar spin ice.

Several important questions are still unresolved regarding the low-temperature physics of the kagome dipolar Ising antiferromaget. What is essentially missing is a Monte Carlo simulation throughout the whole temperature range, especially to confirm [98][2] or infirm that the current candidate for the long range ordered ground state is actually the ground state. Another central question Monte Carlo simulations could answer is the possible existence of phase transitions at low temperature [98].[2] We might expect at least one phase transition from the spin ice phase to the long range ordered ground state. But like the kagome dipolar spin ice, we cannot exclude the existence of an intermediate phase transition, which could, for example, describe a spin liquid state sitting on top of an antiferromagnetic pattern of charged lines (see Fig. 10d).

3.5 The artificial square spin system

So far, we only considered the kagome geometry. However, the square lattice has been extensively studied as well since the seminal paper of Wang et al. [18]. One of the initial motivations in fabricating a square arrangement of interacting nanomagnets, as the one illustrated in Figure 11a, was to mimic the properties of pyrochlore spin ice materials [90], and to visualize in real space how the nanomagnets accommodate the geometrical frustration [18]. Otherwise said, such a square arrangement was expected to behave as a spin liquid, and more specifically

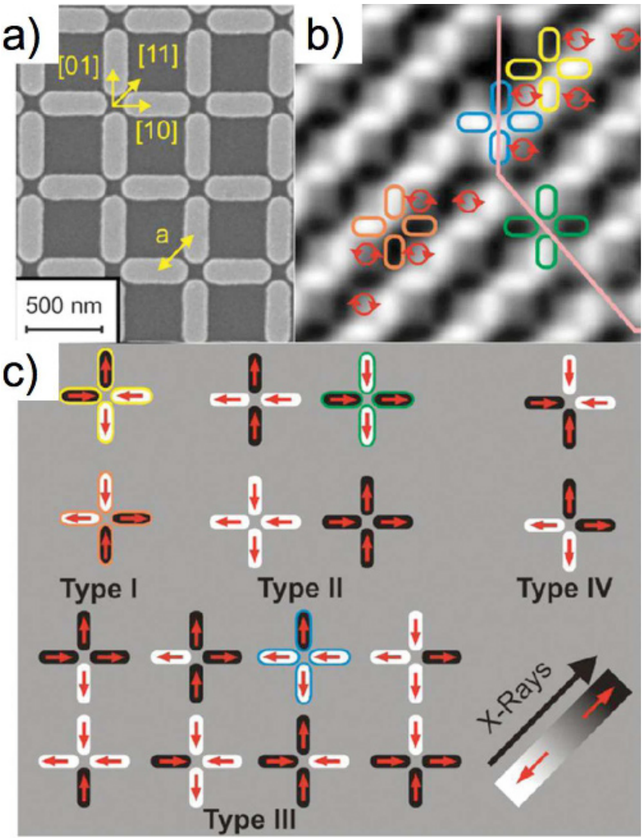

Fig. 11. (a) Scanning electron microscope image of an artificial square spin system. (b) Magnetic image providing the local direction of magnetization and allowing to resolve all vertex configurations. (c) Schematics of the different vertex types and their associated magnetic contrast. Type I vertices, which have the lowest energy, are highlighted in orange and yellow. One type II vertex and one type III vertex, which can be observed in (b), are also highlighted in green and blue, respectively (from Ref. [53] © 2013 the American Physical Society).

as a Coulombic spin liquid (see Sect. 4 for more details). But in contrast with the kagome geometry, the nonequivalent nature of the magnetostatic interactions between nearest neighbors in the square lattice lifts the degeneracy of the expected disordered ground state manifold (we will come back to that point in Sect. 4.2). These artificial realizations were then unsuccessful in achieving a spin liquid state, until recently [99]. Instead, artificial square arrays show a conventional Néel ordering from a high temperature paramagnetic phase to an antiferromagnetic state at low temperature [48,53,61,64,68]. This antiferromagnetic ground state is characterized by a flux closure of magnetic loops with alternating chirality, as shown in Figures 11b and 11c.

For the purpose of this paper, this square arrangement is less interesting for investigating exotic states of matter or cooperative magnetic phenomena. Nevertheless, it is worth mentioning that it is precisely because the system first failed to capture a liquid-like physics that it triggered a wealth of studies and opened the field of artificial spin systems. In particular, the well-defined antiferromagnetic ground state was used as a target configuration for:

- improving the efficiency of demagnetization protocols [33,35,38,48];
- optimizing the magnetic properties of the constituent material [59,61,68];
- characterizing the role of the intrinsic disorder [46,100,101];
- studying thermal fluctuations [64,102] and magnetization reversal processes [103–106];
- or understanding how charged excitations move in an otherwise uncharged but ordered background [107,108];
- just to name a few selected examples. In addition, results on square arrays inspired the community for designing other lattice geometries (see Sect. 3.6) to recover the macroscopic degeneracy of the ground state manifold expected initially.

We note that artificial arrays like the one reported in Figures 11a and 11b are often referred to as artificial square ice systems. This semantic might be confusing in condensed matter physics. The reason is twofold:

- The square ice usually refers to a vertex model of statistical mechanics (also called the six vertex model) which is characterized by a residual entropy at 0 K [85,109]. In this vertex model, over the 16 possible vertex configurations (see Fig. 11c), only the six vertices associated with two spins pointing inwards and two spins pointing outwards (type I and type II vertices) are considered: this is the ice rule constraint. These six vertices are supposed to have the same energy and the 10 remaining vertices (type III and type IV) are disregarded. In *all* the artificial arrays of nanomagnets fabricated so far, these assumptions are not valid: either type I and type II vertices have different energy, or type III vertices remain present.
- As mentioned above, the square ice model is a vertex model, while artificial arrays of nanomagnets are experimental realizations of spin models. This is so because artificial spin systems are made from arrays of magnetic islands that interact through magnetostatics. These arrays are thus assemblies of interacting magnetic elements that mimic pseudo-spin lattices. The energy of a given spin microstate is then the sum of all pairwise spin configurations, in contrast with vertex models, in which the energy of a given microstate is the sum of all individual vertex energies.

To avoid confusion in the following, we will refer to the artificial square spin system (and not square ice) when describing an array as the one shown in Figure 11a.

We might have left the impression that no collective phenomenon takes place in the artificial square spin system. This is not quite true. In particular, although the system orders at low temperature, reaching the ground state requires collective motions of spins: once the temperature prevents the formation of charged local configurations (type III and type IV vertices), only loop and/or

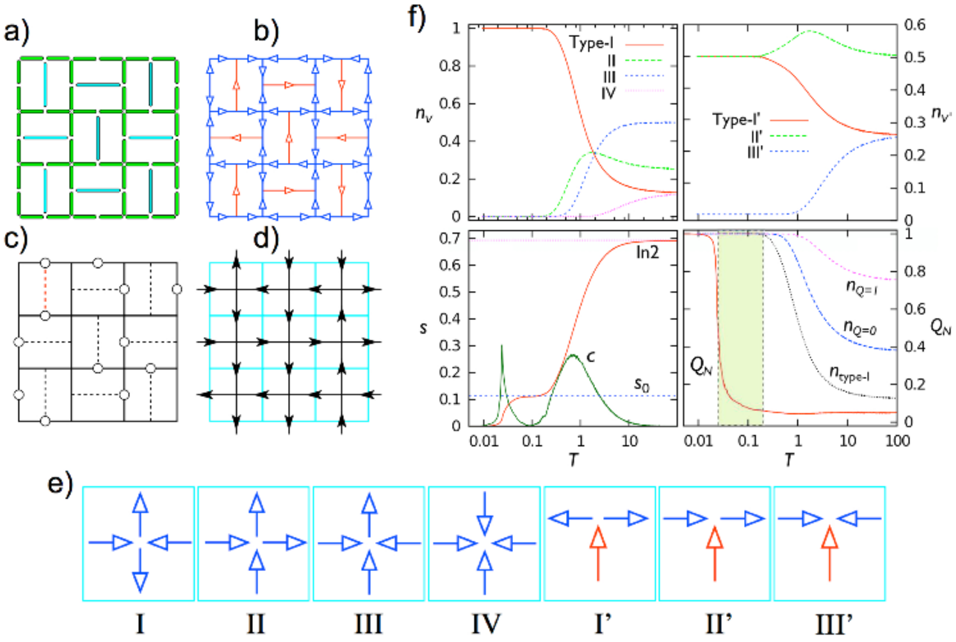

Fig. 12. (a) Lattice geometry of the Shakti spin system. Each green element is an in-plane magnetized nanomagnet. (b) Example of a spin configuration in the Shakti spin system. All square vertices have a type I configuration, while the T-shape vertices, defined by two blue and one red arrows, are either of type I′ or type II′. (c) Vertex configuration associated with the spin state shown in (b). Type II′ vertices are indicated by circles. (d) The vertex configuration in (c) can be mapped on an emergent 6 vertex model. (e) The seven types of vertices for the square and T-shape vertices. (f) Monte Carlo simulations of the Shakti spin system provide the temperature dependence of the vertex populations (top two panels), of the entropy density s and specific-heat c (bottom left panel), and of the order parameter Q_N characterizing the Néel-type charge order in the ground state (from Ref. [111] © 2013 the American Physical Society).

cluster moves allow the conversion of the remaining type II vertices into type I vertices. The spin dynamics is thus intrinsically collective, at least from the model point of view [110].

3.6 Other geometries

As illustrated in the previous sections, artificial arrays of nanomagnets can be used to capture and study disordered magnetic states of matter often associated with frustrated spin systems. In that context, one of the main interests of using such arrays is their flexibility in designing almost any type of two-dimensional arrangement, whether this arrangement exists or not in nature. Among the recent attempts to recover the ground state degeneracy of the square ice model, which is lacking in the artificial square spin system, another lattice topology has been proposed [111,112]. In this so-called Shakti lattice, the nanomagnets are arranged in such a way that the vertices have mixed coordination numbers three and four (see Figs. 12a–12d). Like in the square spin system, the nanomagnets are in-plane magnetized and the magnetization axis is defined by the long axis of the magnetic elements (see magnetic configuration in Fig. 12b). Type I vertices (see Figs. 11c and 12e) are then energetically more favorable for vertices with coordination number four, because of the nonequivalent strengths of the magnetostatic interaction coupling collinear and orthogonal nanomagnets. For the very same reason, T-shape vertices with coordination number three are energetically more favorable if the two collinear nanomagnets are in a head-to-head or tail-to-tail configuration (type I′ vertices, see Fig. 12e). If we now assume that the energy hierarchy between all different vertex types is such that:

$$\epsilon_I < \epsilon_{II} < \epsilon_{III} < \epsilon_{IV}$$
$$\epsilon_{I'} < \epsilon_{II'} < \epsilon_{III'}$$
$$\epsilon_{II'} - \epsilon_{I'} < \epsilon_{II} - \epsilon_I$$

then at zero temperature, vertices with coordination number four have no other choice than being in a type I configuration, while T-shape vertices cannot all have a low-energy type I′ configuration [111,112]. In other words, the square vertices are all in a well-defined state (type I), while the T-shape vertices are either in a type I′ or a type II′ state (with 50%/50% fraction per plaquette, see top right panel in Fig. 12f). The lattice topology thus leads to an interesting observation: the geometrical frustration, i.e., the impossibility to minimize simultaneously all pairwise spin interactions, together with the energy hierarchy mentioned above, translate into a vertex frustration. At low temperature, T-shape vertices cannot be all simultaneously in the lowest possible energy configuration.

This result is important as it provides means to restore a ground state degeneracy in a square-based lattice. In fact, a direct mapping can be made between the Shakti lattice and the square ice model by associating the respective positions of the T-shape type I′ and type II′ vertices with the type I and type II vertices of the square ice (see Figs. 12c and 12d). This mapping has been confirmed by Monte Carlo simulations which show that, within a temperature window, the system highly fluctuates and is characterized by a macroscopic degeneracy (see bottom left panel in Fig. 12f). Although not directly the square ice model, the Shakti lattice provides an alternative way to achieve the ground state degeneracy of the square ice, but in an emergent form [112]. In particular, spin–spin correlations in this emergent form of the square ice reveal the expected algebraic decay [111] (see also Sect. 4).

Besides the Shakti lattice, other lattice topologies have been proposed to investigate disordered magnetic states [113–116]. For example, the tetris lattice also exhibits interesting properties: its low-energy manifold (not shown) consists of alternating ordered and disordered stripes, the latter being described by a one-dimensional Ising model at a fictional temperature [117]. The tetris lattice thus provides means to reduce the dimensionality of the physical behavior via vertex frustration [117]. Besides their own exotic properties, these lattice topologies illustrate once more the strength of being able to design almost any type of two-dimensional lattice that can serve as an experimental platform to bridge concepts from condensed matter physics, nanomagnetism, statistical thermodynamics, vertex and loop models.

4 Coulomb phase in artificial spin systems

In the previous section, we provided several examples of artificial spin systems behaving as spin liquids, and we briefly described the temperature dependence of the spin–spin correlations that develop in these so-called cooperative paramagnets. The kI antiferromagnet (see Sect. 3.2) is the canonical case of a spin liquid with exponentially decaying pairwise spin correlations and an associated correlation length of the order of one lattice constant. The kagome dipolar spin ice (see Sect. 3.3) or the Shakti spin system (see Sect. 3.6) however are spin liquids at low temperature with power-law decaying pairwise spin correlations. Counterintuitively, the correlation length in these algebraic spin liquids is infinite, although the system fluctuates in the manner of a paramagnet.

Besides pairwise spin correlations, the lattice topology together with the local constraints associated with the energy minimization can lead to additional properties. More specifically, certain spin liquids can be seen as a coarse grained, spatially fluctuating magnetic field that obeys the laws of magnetostatics. When this is so, spin liquids are often referred to as Coulombic spin liquids. The purpose of this section is to describe the properties of Coulombic (Ising-like and classical) spin liquids, and to understand to what extent such a magnetic state of matter can be imaged using the lab-on-chip approach offered by artificial spin systems.

We first recall the main ingredients needed to observe a Coulomb phase and the basic features allowing its measurement (Sect. 4.1). We then show why the artificial square ice is a natural candidate for a Coulombic spin liquid (Sect. 4.2), why it is tricky, but possible, to image an artificial Coulombic spin liquid (Sect. 4.3), and why this Coulombic liquid can host magnetic charge defects that behave as classical analogues of magnetic monopoles (Sect. 4.4).

4.1 What is a Coulomb phase?

The concept of Coulomb phase has been introduced by Henley [118] to describe the properties of certain lattice models (i.e., discrete models) using the fundamental laws of electrostatics (or magnetostatics). Otherwise said, a Coulomb phase is an emergent state for lattice models, i.e., a state which is not obviously encoded in the physics describing these lattice models, but which emerges, naturally, after reformulating this physics. Although the concept is quite general and applies to different types of lattice models satisfying a set of three conditions (see below), we only consider here lattice spin models. According to Henley [118], the three conditions for a Coulomb phase are:

Condition 1: each lattice variable (the spin in our case) can be mapped to a discrete signed (magnetic) flux $\mathbf{p}_i$, running along bond i;

Condition 2: at each lattice vertex, the sum of these signed fluxes is zero;

Condition 3: the system is in a highly disordered state (i.e., liquid-like).

Coarse graining these lattice fluxes leads to a vector field $\mathbf{P}(\mathbf{r})$, having the mean value of all the fluxes embedded within a volume V centered at $\mathbf{r}$, V being large compared to the lattice constant, but much smaller than the system size. Assuming that the vector field $\mathbf{P}(\mathbf{r})$ is static (i.e., there is no dynamics in the spin lattice) but spatially fluctuating, Henley showed [118] that $\mathbf{P}(\mathbf{r})$ is divergence-free:

$$\nabla \cdot \mathbf{P}(\mathbf{r}) = 0 \tag{6}$$

and that the free energy F of such a spin lattice has the following form:

$$F/T = \text{const} + \int \frac{1}{2} K |\mathbf{P}(\mathbf{r})|^2 d^2\mathbf{r} \tag{7}$$

with K a constant and T the temperature. These two equations ressemble the energy density of a magnetic field and its divergence constraint in absence of magnetic charge. Starting from a spin model on a lattice, we end up with a coarse grained (continuous) physics that shares common features with magnetostatics. Besides the elegance of the analogy, this magnetostatic framework has important consequences. First, the real space correlations of the vector field $\mathbf{P}(\mathbf{r})$ have the spatial dependence of a dipole–dipole interaction at large distances [119]. Second, local spin configurations that violate the divergence-free condition then behave as sinks or sources of magnetic flux, i.e., as effective (magnetic) charges with Coulomb-like interactions.

We point out here that Coulomb phases are not restricted to spin ice systems and can be found in other three-dimensional or two-dimensional spin liquids. For example, Coulomb phases are also found in Heisenberg antiferromagnets on the kagome [120], checkerboard [121] and pyrochlore [122] lattices. Notably, for spin ice systems, because spins are Ising-like magnetic moments, the magnetic fluxes at each lattice vertex are parallel to the local magnetic moments, so that the vector field $\mathbf{P}(\mathbf{r})$ is directly proportional to the magnetization [118]. For spin ice systems, the algebraic field–field correlations are then also the spin–spin correlations, while they are in general distinct in the Heisenberg antiferromagnets mentioned above.

One might wonder why a highly disordered spin system, characterized by a massively degenerate ground state manifold, and thus a nonzero entropy per spin at very low temperature, could have long range pairwise spin correlations. In other words, one could wonder how a spin system often called a cooperative paramagnet or, equivalently, a spin liquid, could be such that spins communicate at large distances. A useful picture to capture this phenomenon [74] is to remember that the magnetic flux lines at the lattice vertices may never start or end, because of the strong constraint that applies locally on the flux divergence (there is no source or sink of extra magnetic charge above the charged or uncharged vacuum describing the low-energy manifold). Flipping one single spin in the lattice may thus be forbidden, but one other way the system may still be able to fluctuate is to reverse an assembly of spins making a closed loop that preserves the divergence-free constraint. Such loops can be built up with a few spins only, but can extend throughout the entire lattice as well. These loop moves can then potentially propagate spin correlations over large distances. Coulomb phases, and more generally algebraic spin liquids, are thus systems in which fluctuations are allowed through a loop dynamics, i.e., *collective* motions of spins.

One question one now may ask is ‘what are the experimental signatures of a Coulomb phase?’. Henley [119] and others [120–125] showed that a Coulomb phase/algebraic spin liquids have specific diffraction features. At certain wavevectors in reciprocal space, the magnetic structure factor is non-analytic and exhibits a singularity, which takes the form of a pinch point. A pinch point means that, depending on how the singularity is approached, the intensity of the magnetic structure factor is either strictly zero or finite (see Fig. 13). Since artificial spin systems can be imaged in real space, this real space configuration can be Fourier transformed to obtain the corresponding magnetic structure factor, thus allowing to evidence pinch points (see following sections).

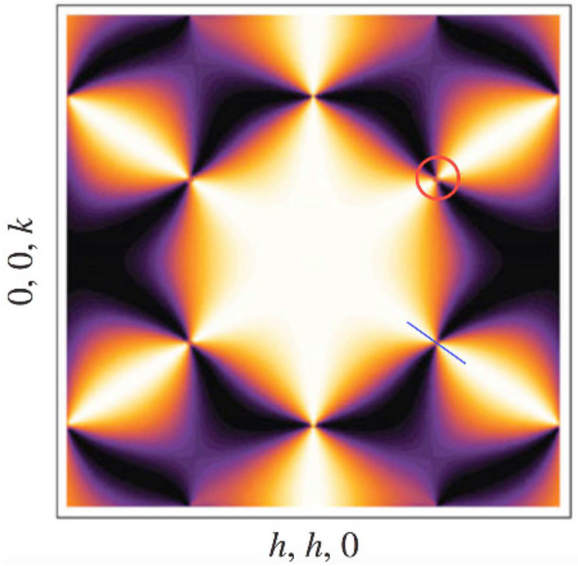

Fig. 13. Magnetic structure factor on the pyrochlore lattice in the [hhk] plane at zero temperature. The location of a pinch point is indicated by a red circle. Along the straight line shown in blue, the intensity is constant when crossing the pinch point, while this intensity is zero when crossing the pinch point in the direction perpendicular to the blue line (adapted from Ref. [126], republished with permission of Royal Society; permission conveyed through Copyright Clearance Center, Inc.).

4.2 The artificial square spin system: a natural candidate to image an arrested configuration of a Coulombic spin liquid?

Another question one may ask is ‘what type of two-dimensional spin model fulfills the three required conditions to observe a Coulomb phase, and which could be fabricated using lithographically patterned arrays of nanomagnets?’ In Section 3, we described several artificial spin systems characterized by a spin liquid state. However, most of the attention in Section 3 was devoted to kagome Ising systems, in which the lattice vertices all carry a magnetic charge. Because of this charged background, artificial kagome systems do not appear as natural candidates to prepare an arrested configuration of a Coulombic spin liquid. Counterintuitively, we will see in Section 5 that a Coulombic spin liquid can in fact be observed in the kagome dipolar spin ice, but this case is quite peculiar and associated to the spin fragmentation process described later.

A natural system that first comes to mind is the artificial square spin system, which was initially fabricated to mimic the intriguing properties of pyrochlore spin ice materials and to explore the physics of the associated six vertex model [18]. As mentioned in Section 3.5, the square spin system consists of (multiaxes) Ising-like, in-plane magnetic moments (see Fig. 11). Each vertex of the lattice has a coordination number of 4 and hosts one of the $2^4 = 16$ possible spin states. These 16 configurations can be classified in 4 different types (see Fig. 11c), having possibly 4 different energies. Among these 16 states, 6 obey the so-called ice rule consisting in two spins pointing in and two spins pointing out at each vertex (type I and type II vertices). In the particular case where type I and type II vertices have the same minimum energy, while type III and type IV vertices correspond to high-energy (and non-observed) states, this 16 vertex model is known as the square ice or six vertex model [85,109].

The square ice model satisfies all three conditions required to observe a Coulomb phase:

(1) the magnetic moments can be mapped to a local signed flux on a lattice (the flux is proportional to the magnetic moment);

(2) each vertex satisfies the zero sum of the four signed fluxes;

(3) the ground state manifold is liquid-like.

As shown in Section 3.5, although conceptually simple, square arrays of interacting magnetic nano-islands reveal a different behavior than the one predicted by the square ice model. This difference is due to the nonequivalent nature of the magnetostatic interactions between collinear and perpendicular nearest neighbors, which lifts the energy degeneracy of type I and type II vertices. This gives rise to an ordered ground state [48,53,61,64,68]. In other words, artificial square spin systems do not mimic the properties of the highly degenerate pyrochlore spin ice materials and cannot be described by the square ice model. Instead, their physics is better described by the F model [127,128] introduced for antiferroelectric crystals and associated to the condition $E_1 < E_2$, where E_1 and E_2 are the energies of type I and type II vertices, respectively. Until recently, all attempts to make an artificial realization of the square ice model were unsuccessful, whether the arrays are field-demagnetized [18,46,100] or thermally annealed [48,53,61,64,68]. More complex topologies involving mixed coordination (such as Shakti lattices, see Sect. 3.6) [111,112] were found to have a high degree of degeneracy and to map on an effective square ice model. However, exotic many-body phenomena such as Coulomb phases and monopole-like excitations on a massively fluctuating uncharged vacuum have not been demonstrated in those experimental realizations.

4.3 Real space imaging of a Coulombic spin liquid

Soon after the pioneering work of Wang et al. [18], Möller and Moessner [129] made a theoretical proposal to recover experimentally the extensive degeneracy of the ground state predicted in the square ice model. This proposal consists in tuning the J_1/J_2 ratio, where J_1 and J_2 are the nearest-neighbor coupling strengths between orthogonal and collinear nanomagnets (see Fig. 14a), by shifting vertically one of the two sublattices of the square array. Doing so increases the distance between orthogonal nanomagnets, while keeping unchanged the distance between collinear nanomagnets. In principle, a vertical shift between the two sublattices of the square array thus allows to vary continuously the J_1/J_2 ratio from its initial value (J_1/J_2 is larger than unity for unshifted sublattices) to zero, when the vertical shift becomes infinitively large. Consequently, a critical value for the vertical shift can be found for which $J_1/J_2 = 1$.

The question then arises of how choosing experimentally the relevant value of the vertical shift h. Several approaches can be followed [129,130], but a natural one when dealing with magnetic nanostructures is to perform micromagnetic simulations. In particular, micromagnetic simulations can use as inputs the real geometrical parameters involved experimentally, such as the length, width, thickness of the nanomagnets and the vertex-to-vertex distance. Besides, they allow taking into account the nonuniform magnetization distribution within the nanomagnets in the estimate of the coupling strength [39]. Results of such simulations reveal that the critical h value required to reach the $J_1/J_2 = 1$ condition is of the order of 100 nm or more for typical dimensions of the nanomagnets [99]. This fairly large value of the shift makes more challenging both the fabrication process and the magnetic imaging of the artificial square ice (see Fig. 14b).

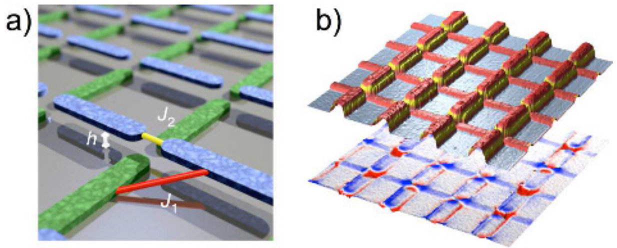

Fig. 14. (a) Schematic of the artificial square lattice in which one (blue) of the two sublattices has been shifted vertically by a height offset h above the other (green). The nearest-neighbor coupling strengths between orthogonal nanomagnets (blue and green; J_1) and collinear nanomagnets (blue/blue or green/green; J_2) are indicated in red and yellow, respectively. (b) Topography (top) and magnetic (bottom) images of an experimental realization of the shifted square lattice. In the topography image, the nanomagnets appear red, the bases used to shift vertically one of the two sublattices are yellow, and the substrate is gray. In the magnetic image, the magnetic contrast appears in blue and red for negative and positive magnetic charges, respectively (from Ref. [99], reprinted by permission from Springer Nature © 2016).

Field demagnetizing a conventional ($h = 0$) and a shifted ($h = 100$ nm) artificial square spin system leads to very different results. In the former case, large patches of the antiferromagnetic ground state, separated by type II domain walls are observed throughout the lattice, consistently with all previous results in the literature. In sharp contrast, the latter case is highly disordered, with a predominance of type II vertices. Type I vertices seem to be diluted and a non-negligible amount of type III vertices is also observed (see Fig. 15a). Clearly, shifting one sublattice of the square array has strong influence on the magnetic configuration observed after a field demagnetization protocol. As mentioned in Section 2.2, the magnetic structure factor is a powerful tool to characterize the order/disorder present in a given magnetic microstate. Doing so on the two artificial arrays shows also striking differences. As expected, the unshifted square array is characterized by magnetic Bragg peaks at the corners of the Brillouin zone, reflecting the antiferromagnetic ordering in real space. For the shifted array however, no magnetic Bragg peaks are observed and the magnetic structure factor is characterized by a diffuse, but structured, background signal (see Fig. 15b). Comparing this result to the predicted magnetic structure factor for the square ice model (see Fig. 15c) reveals strong similarities, suggesting that the artificial square lattice was brought into a spin liquid state.

Moreover, the square ice model is known to be an algebraic spin liquid. As mentioned in Section 4.1, an algebraic spin liquid has features in reciprocal space known as pinch points. These pinch points are clearly visible in the experimental magnetic structure factor shown in Figure 15b. Since the square lattice satisfies all three conditions mentioned in Section 4.1, these pinch points reveal the fingerprint of a Coulomb phase.

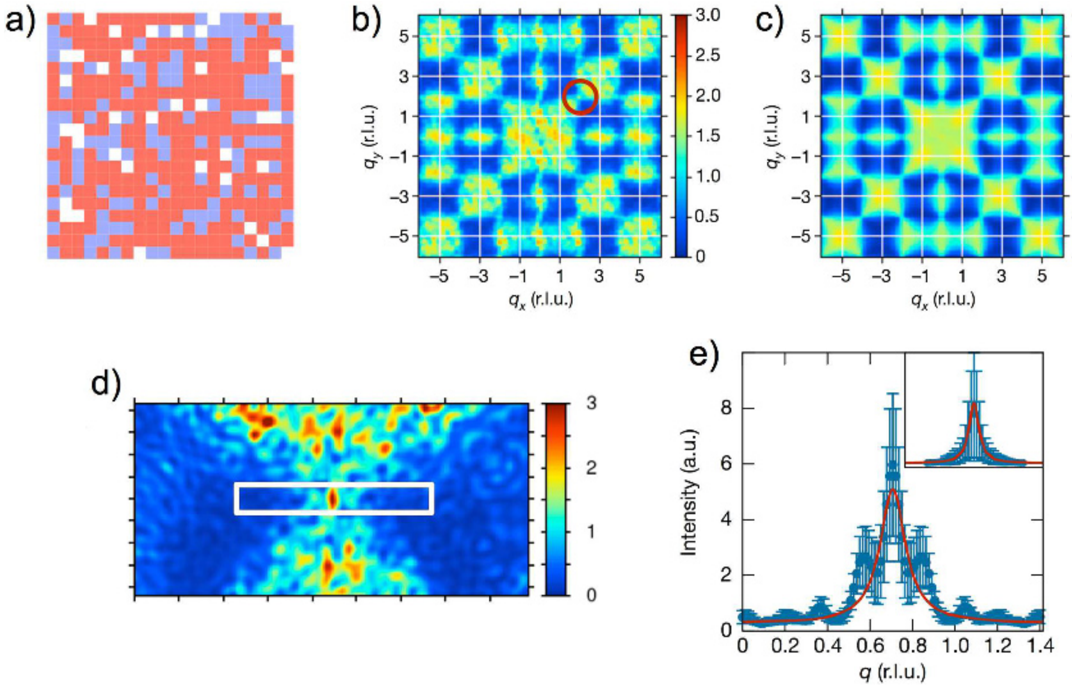

Fig. 15. (a) Real space magnetic configuration of a field demagnetized shifted square lattice in which the height offset is $h = 100\,\text{nm}$. Lattice vertices are colored in blue, red and white for type I, type II and type III, respectively. (b) Magnetic structure factor corresponding to four averaged magnetic configurations similar to the one reported in (a). The color scale refers to the intensity at a given point (q_x, q_y) of the reciprocal space. (c) Computed magnetic structure factor averaged over 1000 random and decorrelated spin configurations that satisfy the ice rule constraint. (d) Zoom of the region indicated by a red circle in (b) showing an experimental pinch point. The q axes correspond to a scan from (3/2, 5/2) to (5/2, 3/2) in reciprocal space. (e) Experimental (main plot) and theoretical (inset) intensity profiles across the pinch point averaged over the white rectangle in (d). The error bars represent the standard deviation calculated from four demagnetizations for the experimental data and from 1000 random ice-rule configurations for the theoretical data. The red curves are single-peaked Lorentzian fits of the pinch points. r.l.u., reciprocal lattice unit; a.u., arbitrary units (from Ref. [99], reprinted by permission from Springer Nature © 2016).

Going back to the real space image, one can conclude that Figure 15a is a snapshot of a spin configuration representative of an algebraic spin liquid. It is worth emphasizing that the vertex populations are not exactly those we would expect within the ground state manifold. Besides the fact that a significant amount of type III defects are trapped in this configuration (white vertices in Fig. 15a), the ratio between type II and type I vertices is not the one expected (~ 2). Nevertheless, the experimental magnetic structure factor shows striking similarities with the one predicted in the ground state manifold of the square ice model. Although the system is not in its ground state, the snapshot shows all the incipient features of a Coulomb phase.

4.4 Monopole-like excitations trapped within a Coulombic spin liquid

As shown above, real space magnetic imaging of a field-demagnetized artificial square ice system reveals the presence of a significant amount of monopoles embedded within a Coulombic spin liquid. Note that this statement is made possible because the spin configuration is resolved both in real space (unambiguous visualization of type III vertices, see Fig. 15a) and in reciprocal space (clear evidence of a Coulomb phase, see Fig. 15b). In fact, the monopole density can be determined exactly for a given snapshot and is found to be of the order of 9% when comparing several snapshots resulting from successive field protocols [99]. Because of this nonzero density of monopoles, the artificial square ice has not been brought, strictly speaking, into the macroscopically degenerate manifold of the corresponding six vertex model. This difference between the (Lieb) ice manifold and the imaged spin configurations of a Coulomb phase with trapped monopoles can be rationalized through the analysis of the pinch point width (Figs. 15d and 15e). This width can be linked to a correlation length ξ, which can be extracted from a Lorentzian fit to the intensity profile passing through a pinch point (Fig. 15d) [131]. Doing so, a correlation length ξ of the order of a fraction of the lattice size is found [99]: $\xi_{\text{theo}} \sim 5$ in lattice constant units for the Lieb ice manifold, while the experimental scan displays a broader peak associated to a shorter correlation length $\xi_{\text{exp}} \sim 4$ (Fig. 15e). The impact of the presence of magnetic monopoles experimentally thus reduces slightly the correlation length in the system, but preserves all the features expected from the six vertex model.

The monopoles imaged in the artificial square ice (see white vertices in Fig. 15a) differ substantially from the charge defects previously reported in artificial square spin systems [53,107,108,110,132–134]. The important

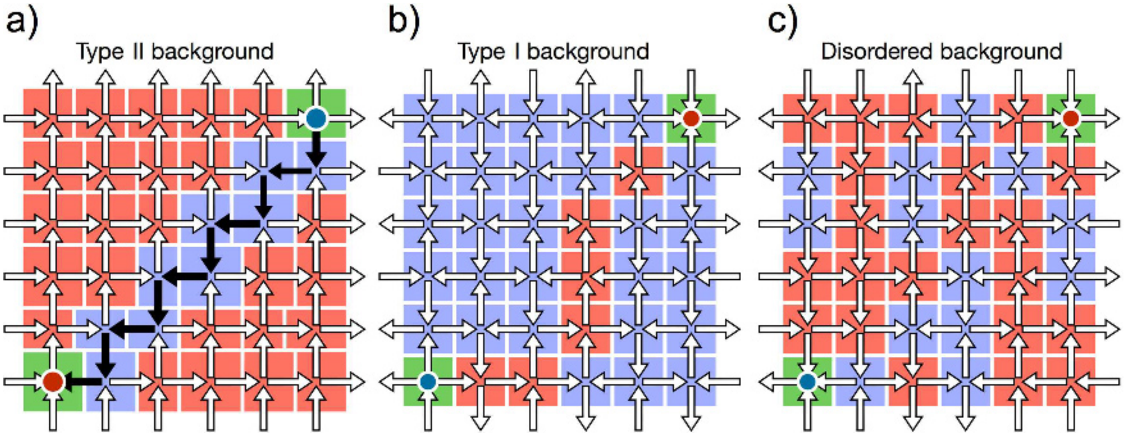

Fig. 16. Pair of oppositely charged defects (red and blue circles) in a magnetically saturated background [type II background; (a)], in the antiferromagnetic ground state [type I background; (b)] and within a disordered manifold [disordered background; (c)]. Blue, red and green squares indicate type I, II and III vertices, respectively. The white arrows give the local spin direction. The black arrows in (a) illustrate a chain of reversed spins (from Ref. [99], reprinted by permission from Springer Nature © 2016).

difference is that monopoles in artificial square ice are particule-like excitations that evolve within a liquid phase, i.e., within a highly disordered manifold, while charge defects live on a magnetically ordered background in artificial square spin systems. In the former case, the excitations behave as *deconfined* quasi-particules which interact via a Coulomb potential, while in the latter case they behave as *confined* quasi-particules linked by a string tension [110,113,132,133]. In fact, several cases may be distinguished.

The first observation of charge defects in the artificial square spin system was achieved after saturating an array with a magnetic field applied along a (11)-like direction, and by subsequently applying a field in the opposite direction with an amplitude close to the coercive field. The protocol then induces the nucleation of charge defects and triggers an avalanche process [107]. This leads to a unidirectional motion of the defects that leave behind them chains of reversed spins often referred to as Dirac strings (see Fig. 16a). Similar results have been obtained in thermally active arrays that have been first magnetically saturated [53]. There, charge defects are embedded within a magnetically saturated state, i.e., a spin configuration containing mainly type II vertices (see Fig. 16a). They are not magnetic monopoles in the sense of Castelnovo et al. [94].

The second observation of charge defects in artificial square spin systems was done in arrays approaching the antiferromagnetic ordered ground state after being demagnetized or annealed [53]. In that case, defects do not necessarily move along straight lines, but are always confined within a domain boundary separating anti-phase ground state domains made of type I vertices (see Fig. 16b). In this case as well, they evolve within an ordered magnetic configuration characterized by a magnetic structure factor that only contains magnetic Bragg peaks. They are not free particles but topological defects allowing antiferromagnetic domains to grow by permitting the motion of domain walls.

The artificial square ice has a distinct behavior: the magnetic charges are *free* to move into a spin liquid state, and are monopoles in the sense of Castelnovo et al. [94]. This situation is illustrated in Figure 16c, where a monopole/antimonopole pair is present within a disordered magnetic configuration characterized by a diffuse magnetic structure factor similar to the one reported in Figure 15c. In sharp contrast with the two other cases described above, the magnetic history which leads to the formation of this pair of oppositely charged monopoles is lost: we cannot identified the chain of spin reversal that occurred to separate these two charges. In fact, with this snapshot alone, many different paths can be chosen arbitrarily to recombine the two magnetic monopoles. Otherwise said, the trace of reversed spins that leads to the deconfinement of the monopole/antimonopole pair has been erased by the magnetic disorder, and there is no obvious mean to know what was the trajectory of these two quasi-particules. One immediate consequence resulting from this impossibility to track back their motion is that oppositely charged monopoles cannot be paired.

In the artificial kagome dipolar spin ice, charge defects can also be studied, although they present less exotic properties. Their first experimental observation was made in conditions similar to the first case mentioned above for the square lattice. Initially saturated, a magnetic field is applied to nucleate a few reversals that subsequently propagate through a unidirectional avalanche process [135–141]. However, because of the charged nature of the vacuum on which these charge defects move, they can quickly annihilate, such that the avalanche process is in fact a periodic sequence of nucleation/propagation events every two spin flips. An alternative description of the avalanche mechanism is to consider the magnetic charge transferred between two neighboring sites and not the absolute value of the local magnetic charge. In that case, the pair of charge defects is also described by a line tension as it evolves within an ordered background. When these charges live on a disordered background, the pairing of oppositely charged defects is not possible and charges may be seen as monopoles. But from our point of view, the physics of those monopoles in kagome lattices is less rich than their counterparts in the square ice because they do not live on a Coulomb phase. Nevertheless, their properties have been extensively investigated for their micromagnetic properties. In particular, several works considered these defects as (chiral) magnetic domain walls propagating in branched arrays of nanostructures [142,143], which in turn shed light on how artificial arrays of nanomagnets demagnetize under an applied magnetic field or a thermal protocol [144–150].

5 Fragmentation of magnetism in the artificial kagome dipolar spin ice

We showed in Section 3.3 that the kagome dipolar spin ice presents a rich phase diagram with intriguing magnetic properties. In particular, the so-called spin ice II phase is characterized by a very unusual behavior: magnetic order and magnetic disorder coexist within a finite temperature window. This coexistence of order and disorder can be visualized in real space: although a magnetic configuration belonging to the spin ice II phase does not show any obvious ordered spin pattern, the magnetic charge associated with the dumbbell description of the magnetic moment does crystallize. As the concept of magnetic charge is directly linked to the magnetic moment, charge ordering implies spin ordering. The spin ice II phase is thus doubly constrained; if all vertices have to satisfy the (kagome) ice rule constraint (two spins pointing inwards and one spin pointing outwards, or vice versa), the ice rule constraint is itself constrained: if two spins point inwards at a given vertex, two spins *must* point outwards at the three neighboring vertices. The magnetic properties of the spin ice II phase are then puzzling in several aspects:
– spin order does exist, but we do not see it, at least not (easily) in real space.
– spin order is only partial since the spin ice II phase is a spin liquid (it has a residual entropy, see Fig. 7a).
– spin order and spin disorder coexist at thermodynamic equilibrium.

In fact, we will show below that it is very difficult to get a mental representation of this unconventional state of matter, especially because each single spin in the lattice contributes at the same time, and everywhere, to the magnetic order and to the magnetic disorder. Thus, we are not discussing here the trivial case of coexisting, out-of-equilibrium magnetic phases. We are neither discussing cases where one sublattice could behave as a paramagnet and one other sublattice could be magnetically ordered [151]. What we will describe in that section is a dynamical, collective state of matter, in which each single classical magnetic moment contributes at the same time to an ordered state and a liquid phase. We will first basically rephrase what is reported in the seminal contribution of Brooks-Bartlett et al., who introduced the concept of magnetic moment fragmentation [76]. Then, we will highlight the most puzzling aspects of the spin ice II phase and show how this phase can be observed in an artificial array of nanomagnets.

5.1 What is spin fragmentation?

The magnetic properties of a spin model are generally well described by the natural degree of freedom encoded in that model: the spin. Otherwise said, to describe the magnetic properties of a given spin model, the natural ingredient to be considered is the spin. This might sound like a tautology, but less common is another level of description, which goes beyond the obvious and is often associated to the concept of emergence. For example, a field is said to be emergent when it is not present in the microscopic model, but arises in an effective theory as an individual or a collective degree of freedom. One such instance of emergence is the recent introduction of classical magnetic monopoles in order to describe the low-energy physics of spin ice materials [94]. Within the associated spin models, the natural excitation is a local spin flip. However, one gains a much deeper understanding of the physics by mapping the spin degree of freedom onto an effective magnetic charge, the emergent field, through a pseudo-fractionalization of atomic magnets into opposite pole pairs [94,152]. In spin ice materials, the success of this mapping is driven by two major ingredients:
(i) any state of the ground state manifold is constrained to have the lattice equivalent of a divergence-free field at each vertex;
(ii) this constraint nevertheless allows this manifold to be massively degenerate.
As a result, the lowest energy spin textures organize themselves as Coulomb phases [118], on top of which the divergence fluctuations relate to a slightly higher energy physics, the one of classical magnetic monopole statistics.

A more general scheme, embracing the previous one, has been proposed recently to describe both aspects of Coulomb phases and geometric organizations of effective magnetic charges [76]. Within this approach, the spin degree of freedom splits into two parts, or fragments, one leading to a divergence-free field and the other one to a divergence-full magnetism, regardless the inner structure of the fields. A striking property of those two fields is the relative independence of their dynamics, leading in some cases to the coexistence of strong spin fluctuations on top of a fragmented-spin crystal [76].

In the kagome dipolar spin ice, spin fragmentation occurs within the spin ice II (SI2) manifold. Any SI2 magnetic configuration may then be mapped onto a global static spin texture coexisting with a fluctuating, even though constrained, magnetic manifold. Algebraically, this corresponds to an Helmholtz decomposition of the total magnetization at each vertex [76]:

$$\sum_{i \in \text{vertex}} \overrightarrow{S}_i = \overrightarrow{\nabla}\phi + \overrightarrow{\nabla} \times \overrightarrow{\mathcal{C}} \tag{8}$$

where $\overrightarrow{S}_i$ is the spin on site i, ϕ a scalar field and $\overrightarrow{\mathcal{C}}$ a vector field. When describing the SI2 phase, the scalar field ϕ is *static*, while $\overrightarrow{\mathcal{C}}$ is a highly fluctuating and collective Coulombic vector field. An example of such a decomposition is given in Figure 17, starting from a spin configuration belonging to the SI2 phase, i.e.,

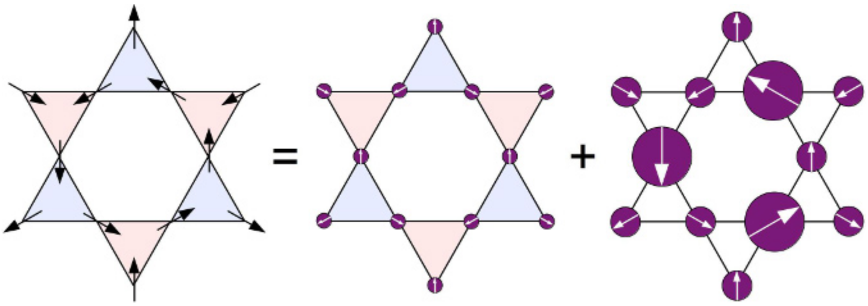

Fig. 17. Illustration of the spin fragmentation process on a small spin cluster belonging to the spin ice II phase. The Ising spins on the kagome lattice are represented by black arrows. The magnetic charges resulting from the dumbbell description of the magnetic moments are represented by red and blue triangles, corresponding to alternating +1 and −1 charged vertices. The Helmholtz–Hodge decomposition applied on this cluster leads to a divergence-full sector and a divergence-free sector. In those sectors, fragmented spins (white arrows) are represented by purple disks of diameters 1/3, 2/3 and 4/3, according to the fraction of the initial magnetic moment they carry (from Ref. [69]).

characterized by a disordered spin state and a magnetic charge crystal. Spins are represented by black arrows, while the associated magnetic charges at the kagome vertices are represented by a red/blue color, corresponding to a +1/−1 charge state, respectively. There, the nearest-neighbor charge–charge correlator is equal to −1, each red triangle being surrounded by three blue triangles, and vice versa. After the Helmholtz decomposition, each spin of the lattice fragments into two parts, such that the magnetic configuration decomposes into a divergence-full and a divergence-free sector. Note that in the two sectors, both the spin direction and the spin length change. To better visualize the fragmentation process, fragmented spins are represented by purple circles of diameter 1/3, 2/3 and 4/3 (see Fig. 17). This type of decomposition can of course be done for any spin configuration belonging to the SI2 phase. The divergence-full part then remains the same and is independent of the initial spin configuration, while the divergence-free part can fluctuate and ensures the magnetic equivalent of a Kirchhoff law (see Fig. 17). Thanks to the massive degeneracy of the SI2 manifold, the $\overrightarrow{\mathcal{C}}$ vector field leads to a Coulomb phase [118].

5.2 Coexistence of spin order and spin disorder: a counterintuitive, collective phenomenon

Another way to visualize the spin fragmentation process is to plot the magnetic structure factor. Its temperature dependence for the kagome dipolar spin ice model has been computed using Monte Carlo simulations (see Fig. 18). Both the SI1 and SI2 phases are characterized by a diffuse background, which becomes more geometrically structured as the temperature is lowered. In the SI2 phase, this geometrical organization is associated to the Coulomb phase coexisting with a fragmented-spin crystal. The ordered part (the ϕ field) results in Bragg peaks, while the dynamic one ($\overrightarrow{\mathcal{C}}$) contributes to a diffuse signal whose algebraic correlations are revealed by the so-called pinch points.

We now examine the properties of the two fragmented sectors in real space to visualize how the spin order looks like. Monte Carlo simulations provide a large number of decorrelated magnetic configurations at a given temperature. For each sampled temperature, these magnetic configurations can all be averaged. If a magnetic order is present, this order should show up in the average configuration. On the contrary, if all these configurations are random or liquid-like, the average configuration should be zero everywhere. Such an analysis has been performed starting from the high temperature regime, where the system is paramagnetic, to the lowest possible temperature, where the kagome dipolar spin ice presents a long range ordered state [81,82]. As expected, in the high temperature paramagnetic regime, each average spin is zero, meaning that the probability for a given spin to be in one direction or the opposite is 50%. Within the spin ice I (SI1) phase, the result is the same (see Fig. 18). Although the phase is constrained and must obey the kagome ice rule everywhere, each spin is zero on average. For the lowest simulated temperatures, the system is ordered and the resulting average configuration reveals the expected LRO pattern [81,82]. The magnetic moment of each spin is one, consistently with the fact that all average configurations provide the same magnetic pattern.

The result is strikingly different in the spin ice II phase. There, the average configuration shows an ordered pattern of all-in/all-out configurations. But the crucial point is that each spin carries only one third of the magnetic moment, contrary to the LRO state in which all spins carry the full magnetic moment. This means that one third only of the magnetism orders, while the two remaining thirds highly fluctuate and give zero signal on the average map. Partial magnetic ordering is then present in the spin ice II phase. The ordered pattern is surprising as it is made of all-in/all-out configurations. We must point out that these configurations are not monopole-like defects as each spin does not contribute to 1, but to 1/3 of the magnetic moment. In other words, in the charge representation, the magnetic charge each vertex carries is not ±3 (i.e., ±1 ± 1 ± 1), but ±1 (i.e., ±1/3 ± 1/3 ± 1/3). The kagome ice rule is thus strictly obeyed in the spin ice II phase. What is puzzling is the all-in/all-out configurations that are usually obtained in antiferromagnetic spin systems. For example, this pattern would not be surprising in a short range kagome spin ice with antiferromagnetic

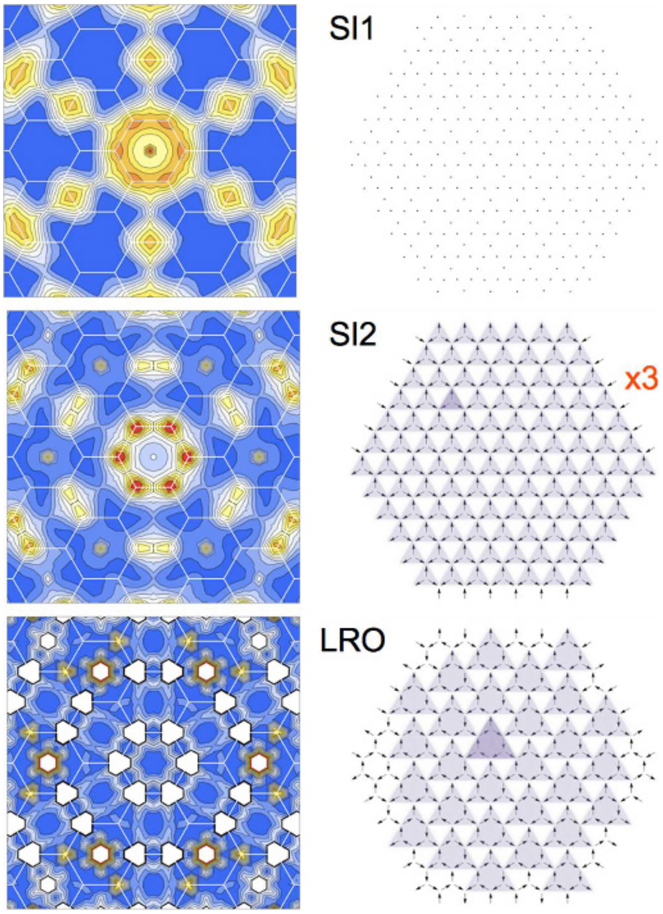

Fig. 18. Magnetic structure factors and their corresponding real space configurations after averaging 10^4 Monte Carlo snapshots for the SI1, SI2 and LRO manifolds. For the magnetic structure factor, blue/red means low/large intensity. Intensity scale is not represented and is different for the three images to better reveal the different features of these two-dimensional maps. In particular, Bragg peaks in the LRO phase appear white since the image has been thresholded. Intensity in these peaks is then intentionally saturated, given an artificial spatial extension. For the real space configurations, the length of the arrows represents the mean value of the local spins after averaging. This length is zero in the SI1, 1/3 of the total length in the SI2 manifold and exactly 1 in the LRO state. The colored triangles give the spin unit cell.

couplings between nearest neighbors. However, in the kagome dipolar spin ice, the coupling between nearest neighbors is ferromagnetic. But again, in this partial order, the kagome ice rule is always satisfied and the observed all in/all out configurations are still compatible with the spin Hamiltonian.

As mentioned above, two thirds of the magnetism are highly fluctuating in the spin ice II phase. This spin liquid is surprising as well, as it exhibits counterintuitive properties. The Helmholtz decomposition shows that this liquid state is made of Ising spins which carry a non-constant magnetic moment. Indeed, the magnetic moment can be either $\pm 2/3$ or $\pm 4/3$ (see Fig. 17). This does not mean that each spin carries either a magnetic moment $\pm 2/3$ or a magnetic moment $\pm 4/3$, but means that each spin can be in one of these 4 states. However, each vertex must satisfy the divergence-free condition resulting from the Helmholtz decomposition, such that each vertex is made of a spin $\pm 4/3$ and two spins $\mp 2/3$. As the system fluctuates, spins can change state but they must do it coherently to obey the divergence-free condition.

The fragmentation of magnetism in thus a collective phenomenon. All spins in the system contribute coherently to the ordered magnetic configuration, for one third, and one third only, of their individual magnetic moment. They also contribute collectively to the fragmented spin liquid, which has to satisfy, everywhere and at any time, the divergence-free condition. In fact, because this fragmented spin liquid satisfies the divergence-free condition, it can be described as a Coulomb phase (see Sect. 4). The fragmented spin liquid is in fact a fragmented Coulombic spin liquid, with algebraic spin–spin correlations and their associated pinch points (see Fig. 18).

5.3 Observation of spin fragmentation

The fragmentation process was evidenced experimentally in two artificial kagome spin ice systems: a thermally active ferrimagnetic alloy with a low Curie temperature (about 250 °C) and an athermal permalloy array which has been field demagnetized [69]. Judging from the real space imaging of these systems, the spin configurations seem essentially disordered and no magnetic pattern appears obviously. To characterize the imaged disorder, the magnetic structure factors were computed for the two systems. In both cases, the corresponding diffraction pattern reveals the coexistence of a diffuse background signal and Bragg peaks in the center of the Brillouin zone. Since these systems have been shown to be well-described by a dipolar spin Hamiltonian at thermodynamic equilibrium, the result strongly suggests that the systems have been trapped within a magnetic configuration that shows the signatures of a fragmented spin liquid.

The magnetic structure factor predicted by Monte Carlo simulations at the effective temperature corresponding to the experimental realization has been used for comparison (see Fig. 19). Although the statistics is low experimentally since the artificial array is made of a few hundreds of nanomagnets only [69], a fairly good qualitative agreement is found with the numerical predictions. In fact, the agreement between the experimental findings and the predictions from the Monte Carlo simulations is semi-quantitative. This can be seen by comparing intensity profiles along certain wavevector directions of the two-dimensional maps. For example, comparison has been made for q-scans running along two axes, the first one passing through both the LRO and fragmented peaks (dotted black line), and the second through the pinch points (continuous black line), along the would be nodal line within the SI2 phase (see Fig. 19b). In these intensity profiles, the q-scans deduced from the Monte Carlo simulations are reported in orange together with the standard deviation associated with the finite size of the system, while the experimental scans appear in light blue.

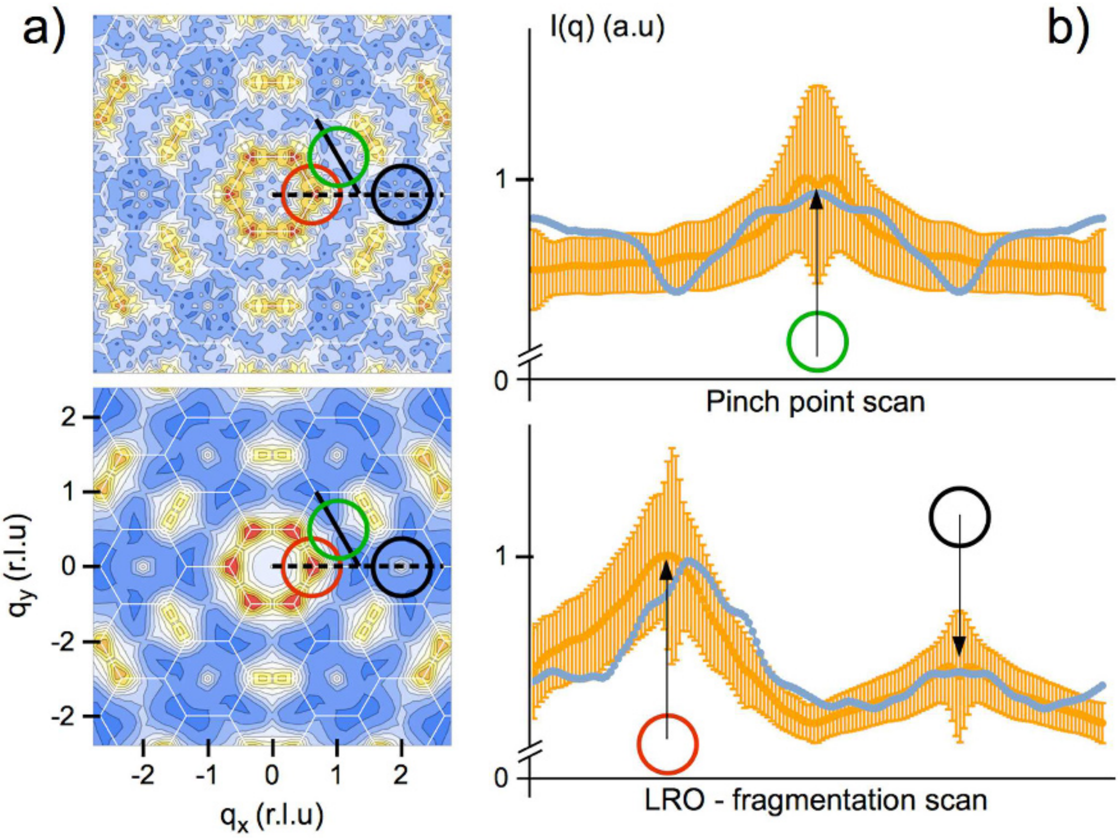

Fig. 19. (a) Experimental (top) and theoretical (bottom) 2D maps of the magnetic structure factor. The position of the Bragg peaks corresponding to the fragmented-spin phase and to the LRO are indicated by a black and a red circle, respectively. Two particular directions in the reciprocal space are indicated by black lines. The pinch point scan (continuous black line) corresponds to the nodal line present in Coulomb phases; the second scan (dotted black line) starts close to the origin of the reciprocal space and passes through first, a LRO q-vector, and then through a fragmentation q-vector. (b) Comparison between the experimental and theoretical q-scans along the 2 directions mentioned before. The dipolar spin ice model captures most features of the spin–spin correlations and agrees semi-quantitatively on the amplitude, as well as on the positions, of the correlations. r.l.u., reciprocal lattice unit; a.u., arbitrary units (adapted from Ref. [69]).

The conclusion here is that the kagome dipolar spin ice Hamiltonian captures every feature of the q-scans and, sometimes, even maps quantitatively onto the measurements, especially through the fragmentation peak. If the agreement with the q-scan running through the pinch point might not be conclusive because of the poor statistics available experimentally, it is still compatible. It has to be emphasized that the experimental and numerical scans have not been scaled one on another: the measured intensity results from the raw data with no particular adjustment.

5.4 Why charge crystallization and spin fragmentation are intimately related phenomena

As we showed above, the fragmented spin crystal is an alternation of all-in/all-out configurations made of spins carrying one third of the total magnetic moment. Consequently, these spin configurations can be represented as an alternation of ±1 magnetic charges at the lattice vertices. The fragmented spin crystal on the kagome lattice can be equivalently described by a perfect ordering of ±1 magnetic charges on a hexagonal lattice. These two equivalent descriptions are illustrated in Figure 17, where the ±1 magnetic charges are represented as red and blue triangles. We emphasize that the magnetic charge has no real meaning and is not encoded in the dipolar spin Hamiltonian of the corresponding model. But since spins and charges are related one another, we can wonder whether the dipolar spin Hamiltonian can be rewritten in such a way that the magnetic charge appears directly. It turns out in the specific case of the kagome dipolar spin ice model that indeed the Hamiltonian can be rewritten, with no approximation, to include the magnetic charge associated with the spins. The key point is to realize that the nearest neighbor charge–charge correlation can be expressed as a linear combination of three spin–spin correlators $C_{ij} = \boldsymbol{S_i}.\boldsymbol{S_j}$. This is so, because the charge-charge correlation links together five different spins, as schematized in Figure 20. These five spins contribute to three different spin–spin correlation coefficients: the nearest-neighbor coefficient $C_{\alpha\beta}$, the next-nearest-neighbor coefficient $C_{\alpha\gamma}$ and the next-next-nearest-neighbor coefficient $C_{\alpha\nu}$. Linking these different terms leads to the following

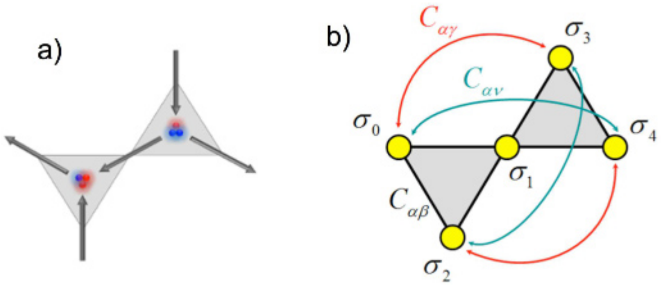

Fig. 20. Schematic representation of the link between the charge–charge correlation coefficient and the spin–spin correlators. (a) A pair of nearest neighboring magnetic charges involves five Ising spins ($\boldsymbol{S}_i = \sigma_i \boldsymbol{e}_i$, with $\sigma_i = \pm 1$ and $\boldsymbol{e}_i$ defining the local anisotropy axis). (b) The configuration of these five Ising variables σ_i can be expressed using the first three spin–spin correlators [$C_{\alpha\beta}$ for the nearest neighbors (in black), $C_{\alpha\gamma}$ for the second nearest neighbors (in red) and $C_{\alpha\nu}$ for the third nearest neighbors (in green)] (from Ref. [69]).

expression for the charge–charge correlation coefficient:

$$Q_u.Q_v = -1 + 8C_{\alpha\beta} + 4C_{\alpha\gamma} - 2C_{\alpha\nu}. \tag{9}$$

Injecting this expression into the spin Hamiltonian provides a new, exact expression, which is now the sum of three different terms:

$$\mathcal{H} = -\tilde{J} \sum_{\langle i,j \rangle} \boldsymbol{S_i}.\boldsymbol{S_j} - \tilde{K} \sum_{\langle u,v \rangle} Q_u.Q_v + O\left(\frac{1}{R^3}\right)|_{R \geq 2r_{nn}}. \tag{10}$$

The first term is a spin Hamiltonian on a kagome lattice coupling nearest neighbors only through a positive coupling constant $\tilde{J}$. This term alone gives rise to a spin liquid. The second term is a charge Hamiltonian on a hexagonal lattice coupling nearest neighboring charges only through a negative coupling constant $\tilde{K}$. This second term alone gives rise to an antiferromagnetic ordering of the magnetic charges on the hexagonal lattice. The third term includes exactly all the remaining terms from the dipolar spin Hamiltonian. Because these three different terms are compatible one another, and because $\mid \tilde{J} \mid > \mid \tilde{K} \mid$, they explain the whole phase diagram of the kagome dipolar spin ice. Starting from the paramagnetic regime and cooling down the system temperature, the physics is dominated by the first term of the Hamiltonian. The system enters the SI1 liquid phase and strictly obeys the kagome ice rule everywhere. As the temperature is further reduced, the second term in the Hamiltonian drives the physics and orders the magnetic charges in an antiferromagnetic fashion. The system is then in the SI2 phase, i.e., the fragmented spin liquid phase. When the system is brought to very low temperature, the third term leads to the long range ordered state.

In other words, if one introduces the concept of magnetic charges, the spin fragmented crystal manifests itself through a magnetic charge crystal. We can then describe the SI2 phase in two equivalent ways. In terms of spin, the SI2 phase is made of the manifold in which the kagome ice rule is strictly obeyed everywhere ($C_{\alpha\beta} = 1/6$ at each vertex sites) *and* in which the linear combination of the first three spin–spin correlators strictly equals -1 everywhere ($-1 + 8C_{\alpha\beta} + 4C_{\alpha\gamma} - 2C_{\alpha\nu} = -1$ for each pair of adjacent vertex sites). This second constraint on the spin arrangement can be expressed as:

$$4C_{\alpha\beta} + 2C_{\alpha\gamma} - C_{\alpha\nu} = 0 \tag{11}$$

$C_{\alpha\beta}$ being a constant (1/6), while $C_{\alpha\gamma}$ and $C_{\alpha\nu}$ are temperature-dependent, i.e., $2C_{\alpha\gamma} - C_{\alpha\nu} = -2/3$ for all temperatures after the SI1/SI2 phase transition.

In terms of spin and charge, the SI2 phase is made of the manifold in which the kagome ice rule is strictly obeyed everywhere *and* in which the magnetic charge has crystallized in an antiferromagnetic fashion. While the first description does not help much to determine visually if an experimental real space snapshot is fragmented, the second description directly gives the answer.

We note that the observation of magnetic moment fragmentation is not specific to artificial kagome spin systems and has also been reported in several compounds [153–156].

6 Concluding remarks and possible future directions

The results obtained these last few years showed that artificial spin systems provide an uncharted area, in which the exotic many-body physics of frustrated magnets can be studied via magnetic imaging techniques, in an almost routine fashion. This capability of artificial spin systems to investigate a wide range of phenomena through a lab-on-chip approach offers the appealing opportunity to test, revisit and extend many theoretical predictions from frustrated spin models. As illustrated in the above sections, artificial spin systems triggered, for example, the discovery of an unconventional state of matter in the dipolar kagome spin ice [39,62,69,76,81,82], the prediction of a complex magnetic order in the dipolar kagome Ising antiferromagnet [92,96,98], and first attempts to explore vertex models from statistical physics [99,111,112,116].

Because artificial spin systems are dipolar, many works allowed to revisit seminal works on spin models, in which nearest-neighbor couplings only were usually considered [79,80,85,89,109,127,128]. It turned out that the dipolar interactions sometimes greatly enrich the physics of the considered system. This is the case for the kagome spin ice: while the short range version of the model gives rise to a conventional spin liquid state with exponentially decaying spin–spin correlations, the phase diagram of the dipolar kagome ice is way more complex and exhibits a fragmented Coulombic spin liquid at low temperatures [76]. It is worth mentioning here that while the short range version of the kagome ice model has been known for quite some time [89], its dipolar version, and the associated new exotic physics, emerged from close interactions between physicists working on highly frustrated magnets and physicists investigating the properties of artificial arrays of magnetic nanostructures. Artificial arrays of nanomagnets are then not just means to test predictions from known models. Precisely because known models could not account for the experimental observations, they were refined and new properties were discovered. Going back to the very first paragraph of the introduction, being able to fabricate a synthetic system to capture a given phenomenon or property is a kind of measure of how deep our knowledge is of this phenomenon or property. Differences between how an artificial system behaves and how it actually behaves in nature or when it is modeled numerically, often lead to very useful pieces of information.

The long range nature of the interaction in artificial spin systems has another important consequence, as these arrays are generally described as vertex systems, especially when considering square-based geometries. For example, if artificial spin systems did not succeed first to capture the extensive degenerate ground state manifold of the six vertex model [85,109], this was done recently [99,112,116]. But it is important to understand that strictly speaking, artificial spin systems should not be described by vertex models but rather by spin Hamiltonians. As a matter of fact, there is a direct link between spin models and vertex models: vertex models are models of statistical mechanics in which a Boltzmann weight is attributed to each vertex of a given lattice, while in their often associated frustrated (Ising) spin models, the Boltzmann weight is attributed to the bond connecting two neighboring vertices. Spin and vertex models are then different types of models. If there is a direct connection between the two when nearest-neighbor interactions only are considered, this connection does not hold anymore in arrays of nanomagnets coupled via magnetostatics.

Designing vertex models is a natural extension of artificial spin systems that would allow to address a physics in which the key ingredient is the energy stored at each vertex site, rather than the two-body magnetic frustration. One possibility is to engineer the frustration in such a way that the overall constraint translates into an emergent vertex frustration (see Sect. 3.6). In that case, vertex models may be used, at least to some extent, to describe a system of nanomagnets interacting through magnetostatics [111,112,157]. Another possibility could be to exploit the micromagnetic nature of the nanomagnets and to store energy in domain walls confined at the vertices of physically connected arrays [158,159]. Interestingly, micromagnetism was essentially neglected so far, except in studies where magnetization reversal, magnetization dynamics and domain wall propagation were considered [142–150,160]. However, micromagnetism offers an extra degree of freedom that might be used conveniently to address the physics of vertex models [158,159]. This extra degree of freedom combined with the possibility to design at will almost any type of two-dimensional lattice might play an important role in the forthcoming investigations.

Further investigations on artificial spin systems can also be made by modifying the design of conventional geometries in order to tune the energy hierarchy of vertices. The idea is somehow similar to the one mentioned just above when using micromagnetism as a knob and has been tested recently [116,161]. In these works, additional nanomagnets are used to control the vertex energies on a square-based geometry to recover the ground state degeneracy of the six vertex model by approaching the $J_1 = J_2$ condition described in Section 4.3. These works provide another instance of the advantage of being capable to engineer the system under investigation to access a given physics. Very likely, this type of approach will be further developed in the future to explore collective phenomena in artificial spin systems.

Most of the existing experimental studies are based on artificial systems in which thermal fluctuations take place on a slow time scale, compatible with the imaging conditions [53,64,117,162]. In the experiments where these fluctuations were accessible, collective phenomena were not directly investigated. Real space imaging of the spin dynamics in the kagome dipolar spin ice or in the artificial square ice would certainly bring important pieces of information. In these two systems, the low-energy dynamics is characterized by loop moves, in which an open or closed loop of spins reverses in a single event. However, this type of collective motion is not possible in an array of magnetic nanostructures, as magnetization reversal takes a certain amount of time before the information is transferred between neighboring elements. Since a very low-energy physics was detected via macroscopic measurements [55,57,163], imaging real time and real space processes could bring new insights into the physics at play.

Although artificial arrays of nanomagnets are meant for engineering frustration and interactions at will, the role of the defects has been essentially unexplored experimentally, except in a recent study [164]. Defects can have different origins. They can be associated to material imperfections, but also to dispersion in island positions, magnetic moments and interactions. To a certain extent, these defects can be designed on purpose by patterning for example arrays with nanomagnets off their ideal positions or by modifying their length to affect their magnetic moment and/or the coupling strength. Defects can also take the form of vacancies by removing a given set of nanomagnets in the lattice [164]. Since the concept of magnetic frustration comes from structurally disordered spin systems, using arrays of nanomagnets to explore the role of defects in artificial spin ice and artificial spin glass systems would be a natural extension of the current works in the field.

Artificial spin systems have also been studied with the idea of reaching exotic low-energy manifolds or capturing particle-like excitations. The two ideas could be combined to study how excitations behave as their density is increased. For example, a rich phase diagram has been predicted for monopoles in the square lattice [134], with a gas of dilute particles changing into a monopole crystal when the density of excitations is sufficiently high. Changing point of view and investigating collective phenomena and phase transitions in the excitation spectrum could be an interesting route to pursue. Besides, tracking the presence of local excitations within crystallites of the kagome spin ice II phase could shed new light on the physics of fragmented spin liquids. Indeed, a local excitation in such a phase should also be fragmented, part of the excitation belonging to the divergence-full sector, and the remaining component belonging to the divergence-free sector. Confining or deconfining such fragmented excitations is a natural, albeit challenging, experimental development, following the preliminary results obtained recently in the dipolar kagome spin ice [69].

Finally, the vast majority of systems that have been studied to date are based on Ising-like pseudo-spins. Few attempts exist where XY pseudo-spins have been fabricated using thin ferromagnetic disks in which in-plane anisotropy can be neglected, thus leading to compass-like lattices [66,165–167], similar to the arrays of macroscopic compass needles [8–10], but at the nanoscale. Investigating frustrated or unfrustrated dipolar spin systems with continuous degrees of rotation might also be an interesting route to follow in the future. More generally, artificial spin systems have largely exploited the possibility to select the lattice geometry and dimensionality [117,168–171], but little has been done so far to engineer the spin degree of freedom. Exploring continuous (such as XY) or discrete (Potts) [172] models might be interesting to connect nanomagnetism and statistical physics, as well as to develop new materials.

We warmly thank all our colleagues and collaborators involved in the original works that allowed writing this review: Y. Perrin, I.-A. Chioar, V.-D. Nguyen, S. Le Denmat, M. Hehn, D. Lacour, F. Montaigne, A. Locatelli, T.O. Menteş and B. Santos Burgos. We also thank the Agence Nationale de la Recherche (ANR), Project No. ANR12-BS04-009 (FRUSTRATED), and the Laboratoire d'excellence LANEF (Grant No. ANR-10-LABX-51-01) for financial support. We acknowledge the support from the Nanofab team at the Institut NEEL.

Author contribution statement

Both authors contributed to the preparation of the manuscript.

References

1. K. Runge, B. Pannetier, EuroPhys. Lett. **24**, 737 (1993)
2. D. Davidović, S. Kumar, D.H. Reich, J. Siegel, S.B. Field, R.C. Tiberio, R. Hey, K. Ploog, Phys. Rev. Lett. **76**, 815 (1996)
3. D. Davidović, S. Kumar, D.H. Reich, J. Siegel, S.B. Field, R.C. Tiberio, R. Hey, K. Ploog, Phys. Rev. B **55**, 214521 (1997)
4. E. Serret, P. Butaud, B. Pannetier, EuroPhys. Lett. **59**, 225 (2002).
5. J.R. Kirtley, C.C. Tsuei, A. Ariando, H.J.H. Smilde, H. Hilgenkamp, Phys. Rev. B **72**, 6518 (2005)
6. J. Trastoy, M. Malnou, C. Ulysse, R. Bernard, N. Bergeal, G. Faini, J. Lesueur, J. Briatico, J.E. Villegas, Nat. Nanotechnol. **9**, 710 (2014)
7. J.-Y. Ge, V.N. Gladilin, J. Tempere, V.S. Zharinov, J. Van de Vondel, J.T. Devreese, V.V. Moshchalkov, Phys. Rev. B **96**, 134515 (2017)
8. E. Olive, P. Molho, Phys. Rev B **58**, 9238 (1998)
9. E.Y. Vedmedenko, H.P. Oepen, J. Kirschner, Phys. Rev. Lett. **90**, 137203 (2003)
10. P. Mellado, A. Concha, L. Mahadevan, Phys. Rev. Lett. **109**, 257203 (2012)
11. E. Ganz, F. Xiong, I.-S. Hwang, J. Golovchenko, Phys. Rev. B **43**, 7316 (1991)
12. J.M. Carpinelli, H.H. Weitering, E.W. Plummer, Surf. Sci. **401**, L457 (1998)
13. B. Ressel, J. Slezák, K.C. Prince, V. Cháb, Phys. Rev. B **66**, 035325 (2002)
14. L. Ottaviano, C. Di Teodoro, S. Santucci, G. Profeta, Phys. Low-Dimens. Struct. 3/4, 149 (2003).
15. L. Ottaviano, B. Ressel, C. Di Teodoro, G. Profeta, S. Santucci, V. Cháb, K.C. Prince, Phys. Rev. B, **67**, 045401 (2003)
16. M. Tanaka, E. Saitoh, H. Miyajima, T. Yamaoka, Y. Iye, J. Appl. Phys. **97**, 10J710 (2005)
17. M. Tanaka, E. Saitoh, H. Miyajima, T. Yamaoka, Y. Iye, Phys. Rev. B, **73**, 052411 (2006)
18. R.F. Wang, C. Nisoli, R.S. Freitas, J. Li, W. McConville, B.J. Cooley, M.S. Lund, N. Samarth, C. Leighton, V.H. Crespi, P. Schiffer, Nature **439**, 303 (2006)
19. A. Libal, C. Reichhardt, C.J. Olson Reichhardt, Phys. Rev. Lett. **97**, 228302 (2006)
20. Y. Han, Y. Shokef, A.M. Alsayed, P. Yunker, T.C. Lubensky, A.G. Yodh, Nature **456**, 898 (2008)
21. C.J.O. Reichhardt, A. Libal, C. Reichhardt, New J. Phys. **14**, 025006 (2012)
22. J. Loehr, A. Ortiz-Ambriz, P. Tierno, Phys. Rev. Lett. **117**, 168001 (2016)
23. A. Ortiz-Ambriz, P. Tierno, Nat. Commun. **7**, 10575 (2016)
24. G. Toulouse, Commun. Phys. **2**, 115 (1977)
25. J. Vannimenus, G. Toulouse, J. Phys. C: Solid State Phys. **10**, L537 (1977)
26. G. Toulouse, in *The Frustration Model* (Springer, Berlin, Heidelberg, 1980), Vol. 115
27. A.Y. Klimenko, Open Thermodyn. J. **6**, 1 (2012)
28. S.T. Bramwell, M.J.P. Gingras, P.C.W. Holdsworth, *Spin Ice* (World Scientific, Singapore, 2013)
29. C. Nisoli, R. Moessner, P. Schiffer, Rev. Mod. Phys. **85**, 1473 (2013)
30. C. Nisoli, Topology by design in magnetic nano-materials: artificial spin ice. arXiv:1711.00921v1 (2017)
31. C.H. Marrows, Experimental studies of artificial spin ice. arXiv:1611.00744v1 (2017)
32. L.J. Heyderman, R.L. Stamps, J. Phys.: Condens. Matter **25**, 363201 (2013)
33. R.F. Wang, J. Li, W. McConville, C. Nisoli, X. Ke, J.W. Freeland, V. Rose, M. Grimsditch, P. Lammert, V.H. Crespi, P. Schiffer, J. Appl. Phys. **101**, 09J104 (2007)
34. C. Nisoli, R.F. Wang, J. Li, W.F. McConville, P.E. Lammert, P. Schiffer, V.H. Crespi, Phys. Rev. Lett. **98**, 217203 (2007)
35. X. Ke, J. Li, C. Nisoli, P.E. Lammert, W. McConville, R.F. Wang, V.H. Crespi, P. Schiffer, Phys. Rev. Lett. **101**, 037205 (2008)
36. E. Mengotti, L.J. Heyderman, A. Fraile Rodriguez, A. Bisig, L. Le Guyader, F. Nolting, H.B. Braun, Phys. Rev. B **78**, 144402 (2008)
37. J. Li, X. Ke, S. Zhang, D. Garand, C. Nisoli, P. Lammert, V.H. Crespi, P. Schiffer, Phys. Rev. B **81**, 092406 (2010)
38. J.P. Morgan, A. Bellew, A. Stein, S. Langridge, C.H. Marrows, Front. Phys. **1**, 28 (2013)
39. N. Rougemaille, F. Montaigne, B. Canals, A. Duluard, D. Lacour, M. Hehn, R. Belkhou, O. Fruchart,

S. El Moussaoui, A. Bendounan, F. Maccherozzi, Phys. Rev. Lett. **106**, 057209 (2011)
40. R.H. Swendsen, J.-S. Wang, Phys. Rev. Lett. **58**, 86 (1987)
41. U. Wolff, Phys. Rev. Lett. **62**, 361 (1989)
42. R.G. Melko, M.J.P. Gingras, J. Phys.: Condens. Matter **16**, R1277 (2004)
43. S.A. Daunheimer, O. Petrova, O. Tchernyshyov, J. Cumings, Phys. Rev. Lett. **107**, 167201 (2011)
44. Z. Budrikis, P. Politi, R.L. Stamps, J. Appl. Phys. **111**, 07E109 (2012)
45. Z. Budrikis, P. Politi, R.L. Stamps, New J. Phys. **14**, 045008 (2012)
46. Z. Budrikis, J.P. Morgan, J. Akerman, A. Stein, P. Politi, S. Langridge, C.H. Marrows, R.L. Stamps, Phys. Rev. Lett. **109**, 037203 (2012)
47. Z. Budrikis, J.P. Morgan, J. Akerman, A. Stein, P. Politi, S. Langridge, C.H. Marrows, R.L. Stamps, Erratum: Disorder strength and field-driven ground state domain formation in artificial spin ice: Experiment, simulation, and theory (vol 109, 037203, pg 2012). Phys. Rev. Lett. 110 (2013)
48. J.P. Morgan, A. Stein, S. Langridge, C.H. Marrows, Nat. Phys. **7**, 75 (2011)
49. J. Cumings, Nat. Phys. **7**, 7 (2011)
50. J.P. Morgan, J. Akerman, A. Stein, C. Phatak, R.M.L. Evans, S. Langridge, C.H. Marrows, Phys. Rev. B **87**, 024405 (2013)
51. A. Farhan, P.M. Derlet, A. Kleibert, A. Balan, R.V. Chopdekar, M. Wyss, L. Anghinolfi, F. Nolting, L.J. Heyderman, Nat. Phys. **9**, 375 (2013)
52. C. Marrows, Nat. Phys. **9**, 324 (2013)
53. A. Farhan, P.M. Derlet, A. Kleibert, A. Balan, R.V. Chopdekar, M. Wyss, J. Perron, A. Scholl, F. Nolting, L.J. Heyderman, Phys. Rev. Lett. **111**, 057204 (2013)
54. A. Farhan, A. Kleibert, P.M. Derlet, L. Anghinolfi, A. Balan, R.V. Chopdekar, M. Wyss, S. Gliga, F. Nolting, L.J. Heyderman, Phys. Rev. B **89**, 214405 (2014)
55. L. Anghinolfi, H. Luetkens, J. Perron, M.G. Flokstra, O. Sendetskyi, A. Suter, T. Prokscha, P.M. Derlet, S.L. Lee, L.J. Heyderman, Nat. Commun. **6**, 8278 (2015)
56. U.B. Arnalds, J. Chico, H. Stopfel, V. Kapaklis, O. Barenbold, M.A. Verschuuren, U. Wolff, V. Neu, A. Bergman, B. Hjörvarsson, New J. Phys. **18**, 023008 (2016)
57. O. Sendetskyi, L. Anghinolfi, V. Scagnoli, G. Moller, N. Leo, A. Alberca, J. Kohlbrecher, J. Luning, U. Staub, L.J. Heyderman, Phys. Rev. B 93, 224413 (2016)
58. S.A. Morley, D. Alba Venero, J.M. Porro, S.T. Riley, A. Stein, P. Steadman, R.L. Stamps, S. Langridge, C.H. Marrows, Phys. Rev. B **95**, 104422 (2017)
59. V. Kapaklis, U.B. Arnalds, A. Harman-Clarke, E.Th. Papaioannou, M. Karimipour, P. Korelis, A. Taroni, P.C.W. Holdsworth, S.T. Bramwell, B. Hjörvarsson, New J. Phys. **14**, 035009 (2012)
60. U.B. Arnalds, A. Farhan, R.V. Chopdekar, V. Kapaklis, A. Balan, E. Th. Papaioannou, M. Ahlberg, F. Nolting, L.J. Heyderman, B. Hjörvarsson, Appl. Phys. Lett. **101**, 112404 (2012)
61. J.M. Porro, A. Bedoya-Pinto, A. Berger, P. Vavassori, New J. Phys. **15**, 055012 (2013)
62. S. Zhang, I. Gilbert, C. Nisoli, G.-W. Chern, M.J. Erickson, L. O'Brien, C. Leighton, P.E. Lammert, V.H. Crespi, P. Schiffer, Nature **500**, 553 (2013)
63. L.J. Heyderman, Nat. Nanotechnol. **8**, 705 (2013)
64. V. Kapaklis, U.B. Arnalds, A. Farhan, R.V. Chopdekar, A. Balan, A. Scholl, L.J. Heyderman, B. Hjörvarsson, Nat. Nanotechnol. **9**, 514 (2014)
65. F. Montaigne, D. Lacour, I.A. Chioar, N. Rougemaille, D. Louis, S. Mc Murtry, H. Riahi, B. Santos Burgos, T.O. Mentes, A. Locatelli, B. Canals, M. Hehn, Sci. Rep. **4**, 5702 (2014)
66. U.B. Arnalds, M. Ahlberg, M.S. Brewer, V. Kapaklis, E.Th. Papaioannou, M. Karimipour, P. Korelis, A. Stein, S. Olafsson, T.P.A. Hase, B. Hjörvarsson, Appl. Phys. Lett. **105**, 042409 (2014)
67. I.A. Chioar, B. Canals, D. Lacour, M. Hehn, B. Santos Burgos, T.O. Mentes, A. Locatelli, F. Montaigne, N. Rougemaille, Phys. Rev. B **90**, 220407(R) (2014)
68. J. Drisko, S. Daunheimer, J. Cumings, Phys. Rev. B **91**, 224406 (2015)
69. B. Canals, I.-A. Chioar, V.-D. Nguyen, M. Hehn, D. Lacour, F. Montaigne, A. Locatelli, T.O. Mentes, B. Santos Burgos, N. Rougemaille, Nat. Commun. **7**, 11446 (2016)
70. M.S. Andersson, S.D. Pappas, H. Stopfel, E. Ostman, A. Stein, P. Nordblad, R. Mathieu, B. Hjörvarsson, V. Kapaklis, Sci. Rep. **6**, 37097 (2016)
71. P. Fendley, J. Phys. A: Math. Gen. **39**, 15445 (2006)
72. C. Nisoli, J. Li, X. Ke, D. Garand, P. Schiffer, V.H. Crespi, Phys. Rev. Lett. **105**, 047205 (2010)
73. J.T. Chalker, Spin liquids and frustrated magnetism, 2010
74. L. Balents, Nature **464**, 199 (2010)
75. G. Misguich, in *Quantum Spin Liquids and Fractionalization in Introduction to Frustrated Magnetism*, edited by C. Lacroix, P. Mendels, F. Mila (Springer, New York, 2011), Vol. 164
76. M.E. Brooks-Bartlett, S.T. Banks, L.D.C. Jaubert, A. Harman-Clarke, P.C.W. Holdsworth, Phys. Rev. X **4**, 011007 (2014)
77. L.D.C. Jaubert, SPIN **5**, 1540005 (2015)
78. G.H. Wannier, Phys. Rev. **79**, 357 (1950)
79. I. Syôzi, Progr. Theor. Phys. **6**, 306 (1951)
80. K. Kanô, S. Naya, Progr. Theor. Phys. **10**, 158 (1953)
81. G. Möller, R. Moessner, Phys. Rev. B **80**, 140409 (2009)
82. G.-W. Chern, P. Mellado, O. Tchernyshyov, Phys. Rev. Lett. **106**, 207202 (2011)
83. J. Villain, Z. Phys. B Condens. Matter **33**, 31 (1979)
84. J.F. Nagle, J. Math. Phys. **7**, 1484 (1966)
85. E.H. Lieb, Phys. Rev. Lett. **18**, 692 (1967)
86. J.D. Bernal, R.H. Fowler, J. Chem. Phys. **1**, 515 (1933)
87. L. Pauling, J. Am. Chem. Soc. **57**, 2680 (1935)
88. A.J. Macdonald, P.C.W. Holdsworth, R.G. Melko, J. Phys.: Condens. Matter **23**, 164208 (2011)
89. A.S. Wills, R. Ballou, C. Lacroix, Phys. Rev. B **66**, 144407 (2002)
90. M.J. Harris, S.T. Bramwell, D.F. McMorrow, T. Zeiske, K.W. Godfrey, Phys. Rev. Lett. **79**, 2554 (1997)
91. R. Moessner, Phys. Rev. B **57**, R5587 (1998)
92. I.A. Chioar, N. Rougemaille, A. Grimm, O. Fruchart, E. Wagner, M. Hehn, D. Lacour, F. Montaigne, B. Canals, Phys. Rev. B **90**, 064411 (2014)
93. Y. Qi, T. Brintlinger, J. Cumings, Phys. Rev. B **77**, 094418 (2008)
94. C. Castelnovo, R. Moessner, S.L. Sondhi, Nature **451**, 42 (2008)

95. S. Zhang, J. Li, I. Gilbert, J. Bartell, M.J. Erickson, Y. Pan, P.E. Lammert, C. Nisoli, K.K. Kohli, R. Misra, V.H. Crespi, N. Samarth, C. Leighton, P. Schiffer, Phys. Rev. Lett. **109**, 087201 (2012)
96. I.A. Chioar, N. Rougemaille, B. Canals, Phys. Rev. B **93**, 214410 (2016)
97. B. Yee, Magnetic ordering of dipolar spin ice in moderate [111] field. http://hdl.handle.net/10012/10803 (2016)
98. J. Hamp, R. Moessner, C. Castelnovo, Phys. Rev. B **98**, 144439 (2018)
99. Y. Perrin, B. Canals, N. Rougemaille, Nature **540**, 410 (2016)
100. Z. Budrikis, P. Politi, R.L. Stamps, Phys. Rev. Lett. **107**, 217204 (2011)
101. Z. Budrikis, Solid State Phys. **65**, 109 (2014)
102. Z. Budrikis, K.L. Livesey, J.P. Morgan, J. Akerman, A. Stein, S. Langridge, C.H. Marrows, R.L. Stamps, New J. Phys. **14**, 035014 (2012)
103. K.K. Kohli, A.L. Balk, J. Li, S. Zhang, I. Gilbert, P.E. Lammert, V.H. Crespi, P. Schiffer, N. Samarth, Phys. Rev. B **84**, 180412(R) (2011)
104. J.P. Morgan, A. Stein, S. Langridge, C.H. Marrows, New J. Phys. **13**, 105002 (2011)
105. C. Phatak, M. Pan, A.K. Petford-Long, S. Hong, M. De Graef, New J. Phys. **14**, 075028 (2012)
106. J. Perron, L. Anghinolfi, B. Tudu, N. Jaouen, J.-M. Tonnerre, M. Sacchi, F. Nolting, J. Luening, L.J. Heyderman, Phys. Rev. B **88**, 214424 (2013)
107. C. Phatak, A.K. Petford-Long, O. Heinonen, M. Tanase, M. De Graef, Phys. Rev. B **83**, 174431 (2011)
108. S.D. Pollard, V. Volkov, Y. Zhu, Phys. Rev. B **85**, 180402(R) (2012)
109. E.H. Lieb, Phys. Rev. **162**, 162 (1967)
110. R.C. Silva, F.S. Nascimento, L.A.S. Mól, W.A. Moura-Melo, A.R. Pereira, New J. Phys. **14**, 015008 (2012)
111. G.-W. Chern, M.J. Morrison, C. Nisoli, Phys. Rev. Lett. **111**, 177201 (2013)
112. I. Gilbert, G.-W. Chern, S. Zhang, L. O'Brien, B. Fore, C. Nisoli, P. Schiffer, Nat. Phys. **10**, 671 (2014)
113. F.S. Nascimento, L.A.S. Mól, W.A. Moura-Melo, A.R. Pereira, New J. Phys. **14**, 115019 (2012)
114. M.J. Morrison, T.R. Nelson, C. Nisoli, New J. Phys. **15**, 045009 (2013)
115. I.R.B. Ribeiro, F.S. Nascimento, S.O. Ferreira, W.A. Moura-Melo, C.A.R. Costa, J. Borme, P.P. Freitas, G.M. Wysin, C.I.L. de Araujo, A.R. Pereira, Sci. Rep. **7**, 13982 (2017)
116. E. Östman, H. Stopfel, I.-A. Chioar, U.B. Arnalds, A. Stein, V. Kapaklis, B. Hjörvarsson, Nat. Phys. **14**, 375 (2018)
117. I. Gilbert, Y. Lao, I. Carrasquillo, L. O'Brien, J.D. Watts, M. Manno, C. Leighton, A. Scholl, C. Nisoli, P. Schiffer, Nat. Phys. **12**, 162 (2015)
118. C.L. Henley, Ann. Rev. Condens. Matter Phys. **1**, 179 (2010)
119. C.L. Henley, Phys. Rev. B **71**, 014424 (2005)
120. D.A. Garanin, B. Canals, Phys. Rev. B **59**, 443 (1999)
121. B. Canals, D.A. Garanin, Eur. Phys. J. B **26**, 439 (2002)
122. B. Canals, D.A. Garanin, Can. J. Phys. **79**, 1323 (2001)
123. J. Villain, Solid State Commun. **10**, 967 (1972)
124. R. Youngblood, J.D. Axe, B.M. McCoy, Phys. Rev. B **21**, 5212 (1980)
125. M.J. Harris, M.P. Zinzin, Mod. Phys. Lett. B **10**, 417 (1996)
126. J. Rehn, R. Moessner, Philos. Trans. R. Soc. A **374**, 20160093 (2016)
127. F. Rys, Helv. Phys. Acta **36**, 537 (1963)
128. E.H. Lieb, Phys. Rev. Lett. **18**, 1046 (1967)
129. G. Möller, R. Moessner, Phys. Rev. Lett. **96**, 237202 (2006)
130. D. Thonig, S. Reißaus, I. Mertig, J. Henk, J. Phys: Condens. Matter **26**, 266006 (2014)
131. T. Fennell, P.P. Deen, A.R. Wildes, K. Schmalzl, D. Prabhakaran, A.T. Boothroyd, R.J. Aldus, D.F. McMorrow, S.T. Bramwell, Science **326**, 415 (2009)
132. L.A. Mól, R.L. Silva, R.C. Silva, A.R. Pereira, W.A. Moura-Melo, B.V. Costa, J. Appl. Phys. **106**, 063913 (2009)
133. R.C. Silva, R.J.C. Lopes, L.A.S. Mól, W.A. Moura-Melo, G.M. Wysin, A.R. Pereira, Phys. Rev. B **87**, 014414 (2013)
134. Y.-L. Xie, Z.-Z. Du, Z.-B. Yan, J.-M. Liu, Sci. Rep. **5**, 15875 (2015)
135. S. Ladak, D.E. Read, G.K. Perkins, L.F. Cohen, W.R. Branford, Nat. Phys. **6**, 359 (2010)
136. E. Mengotti, L.J. Heyderman, A.F. Rodriguez, F. Nolting, R.V. Huegli, H.-B. Braun, Nat. Phys. **7**, 68 (2011)
137. S. Ladak, D. Read, T. Tyliszczak, W.R. Branford, L.F. Cohen, New J. Phys. **13**, 023023 (2011)
138. S. Ladak, D.E. Read, W.R. Branford, L.F. Cohen, New J. Phys. **13**, 063032 (2011)
139. A. Schumann, P. Szary, E.Y. Vedmedenko, H. Zabel, New J. Phys. **14**, 035015 (2012)
140. R.V. Huegli, G. Duff, B. O'Conchuir, E. Mengotti, L.J. Heyderman, A.F. Rodriguez, F. Nolting, H.-B. Braun, J. Appl. Phys. **111**, 07E103 (2012)
141. A. Leon, Curr. Appl. Phys. **13**, 2014 (2013)
142. K. Zeissler, S.K. Walton, S. Ladak, D.E. Read, T. Tyliszczak, L.F. Cohen, W.R. Branford, Sci. Rep. **3**, 1252 (2013)
143. N. Rougemaille, F. Montaigne, B. Canals, M. Hehn, H. Riahi, D. Lacour, J.-C. Toussaint, New J. Phys. **15**, 035026 (2013)
144. S. Ladak, S.K. Walton, K. Zeissler, T. Tyliszczak, D.E. Read, W.R. Branford, L.F. Cohen, New J. Phys. **14**, 045010 (2012)
145. Y. Shen, O. Petrova, P. Mellado, S. Daunheimer, J. Cumings, O. Tchernyshyov, New J. Phys. **14**, 035022 (2012)
146. A. Pushp, T. Phung, C. Rettner, B.P. Hughes, S.-H. Yang, L. Thomas, S.S.P. Parkin, Nat. Phys. **9**, 505 (2013)
147. S.K. Walton, K. Zeissler, D.M. Burn, S. Ladak, D.E. Read, T. Tyliszczak, L.F. Cohen, W.R. Branford, New J. Phys. **17**, 013054 (2015)
148. D.M. Burn, M. Chadha, W.R. Branford, Phys. Rev. B **92**, 214425 (2015)
149. K. Zeissler, M. Chadha, E. Lovell, L.F. Cohen, W.R. Branford, Sci. Rep. **6**, 30218 (2016)
150. D.M. Burn, M. Chadha, W.R. Branford, Phys. Rev. B **95**, 104417 (2017)
151. P. Azaria, H.T. Diep, H. Giacomini, Phys. Rev. Lett. **59**, 1629 (1987)

152. C. Castelnovo, R. Moessner, S.L. Sondhi, Ann. Rev. Condens. Matter Phys. **3**, 35 (2012)
153. S. Petit, E. Lhotel, B. Canals, M. Ciomaga Hatnean, J. Ollivier, H. Muttka, E. Ressouche, A.R. Wildes, M.R. Lees, G. Balakrishnan, Nat. Phys. **12**, 746 (2016)
154. O. Benton, Phys. Rev. B **94**, 104430 (2016)
155. J.A.M. Paddison, H.S. Ong, J.O. Hamp, P. Mukherjee, X. Bai, M.G. Tucker, N.P. Butch, C. Castelnovo, M. Mourigal, S.E. Dutton, Nat. Commun. **7**, 13842 (2016)
156. E. Lefrançois, V. Cathelin, E. Lhotel, J. Robert, P. Lejay, C.V. Colin, B. Canals, F. Damay, J. Ollivier, B. Fak, L.C. Chapon, R. Ballou, V. Simonet, Nat. Commun. **8**, 209 (2017)
157. C. Nisoli, V. Kapaklis, P. Schiffer, Nat. Phys. **13**, 200 (2017)
158. V. Schánilec, Y. Perrin, S. Le Denmat, B. Canals, N. Rougemaille, Artificial vertex systems by design. unpublished.
159. Y. Perrin, B. Canals, N. Rougemaille, Proposal to explore different variants of the six-vertex model using artificial square ice systems. unpublished.
160. S. Gliga, A. Kakay, L.J. Heyderman, R. Hertel, O.G. Heinonen, Phys. Rev. B **92**, 060413(R) (2015)
161. A. Farhan, C.F. Petersen, S. Dhuey, L. Anghinolfi, Q.H. Qin, M. Saccone, S. Velten, C. Wuth, S. Gliga, P. Mellado, M.J. Alava, A. Scholl, S. van Dijken, Nat. Commun. **8**, 995 (2017)
162. A. Farhan, A. Scholl, C.F. Petersen, L. Anghinolfi, C. Wuth, S. Dhuey, R.V. Chopdekar, P. Mellado, M.J. Alava, S. van Dijken, Nat. Commun. **7**, 12635 (2016)
163. A. Glavic, B. Summers, A. Dahal, J. Kline, W. Van Herck, A. Sukhov, A. Ernst, D.K. Singh, Adv. Sci. 1700856 (2018)
164. J. Drisko, T. Marsh, J. Cumings, Nat. Commun. **8**, 14009 (2017)
165. M. van Kampen, I.L. Soroka, R. Bručas, B. Hjörvarsson, R. Wieser, K.D. Usadel, M. Hanson, O. Kazakova, J. Grabis, H. Zabel, C. Jozsa, B. Koopmans, J. Phys.: Condens. Matter **17**, L27 (2004)
166. M. Ewerlin, D. Demirbas, F. Brüssing, O. Petracic, A.A. Ünal, S. Valencia, F. Kronast, H. Zabel, Phys. Rev. Lett. **110**, 177209 (2013)
167. N. Leo, S. Holenstein, D. Schildknecht, O. Sendetskyi, H. Luetkens, P.M. Derlet, V. Scagnoli, D. Lançon, J.R.L. Mardegan, T. Prokscha, A. Suter, Z. Salman, S. Lee, L.J. Heyderman, Nat. Commun. **9**, 2850 (2018)
168. R.P. Cowburn, Phys. Rev. B **65**, 092409 (2002)
169. D. Li, C. Yu, J. Pearson, S.D. Bader, Phys. Rev. B **66**, 020404(R) (2002)
170. A. Imre, G. Csaba, G.H. Bernstein, W. Porod, V. Metlushko, Superlattices Microstruct. **34**, 513 (2003)
171. V.D. Nguyen, Y. Perrin, S. Le Denmat, B. Canals, N. Rougemaille, Phys. Rev. B **96**, 014402 (2017)
172. D. Louis, D. Lacour, M. Hehn, V. Lomakin, T. Hauet, F. Montaigne, Nat. Mater. **17** 1076 (2018)